

POLITECNICO DI TORINO

Master of Science in Mechatronic Engineering



**Politecnico
di Torino**

Master's Degree Thesis

DESIGN OF A TEST RIG FOR A LINEAR ELECTRODYNAMIC LEVITATION SYSTEM

Supervisors:

Prof. Andrea TONOLI

Prof. Nicola AMATI

Dr. Angelo BONFITTO

Candidate:

Alessia D'ORONZO

A.Y. 2020/21

Summary

As the climate crisis becomes an increasingly urgent issue, and being the transportation industry one of the main actors in this scenario, a revolution of this sector has become a priority. Numerous research efforts are being made in this direction, among which the magnetic levitation (maglev) train technology draws particular attention, aiming at a fast, reliable and potentially zero-emission transportation system.

Maglev trains, with their ability to reach 600 km/h speeds, represented a promising solution but the costs for reaching this speed, indeed already achievable by plane, were impeding.

In this framework, Hyperloop represents a breakthrough, introducing the concept of capsules traveling in vacuum-sealed tubes without being subject to air friction phenomena, hence being able to reach significant speeds (about 1000-1200 km/h).

Many aspects of this technology, namely the propulsion mechanism, the design and implementation of the infrastructures as well as the aerodynamic behavior of the capsules, have been thoroughly tackled by recent research work, while the enabling mechanism of this technology, the levitation subsystem, is still partially unexplored.

The Politecnico di Torino, along with Hyperloop Transportation Systems itself, is working on this topic, designing, building and testing a test bench that re-enacts the electrodynamic behavior of a Hyperloop-like levitation system, in order to assess the multi-domain model proposed by Galluzzi et al. and validated by Circosta et al. in their research work.

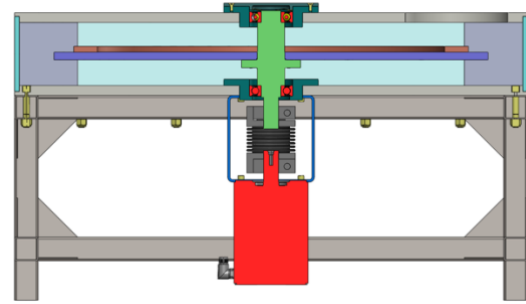
Such an approach consists in combining the accurate eddy currents distribution description in the electromagnetic domain with the variables describing the vertical levitation dynamics of the system, belonging to the mechanical domain. Additional damping is needed to compensate for the inherent instability of such a system.

The core of this thesis work consists in delineating every step of the design process of such bench, starting from a literature analysis whose aim is to explain some of the design choices made, then describing the different aspects of the two final systems, one designed to run the quasi-static analysis and the other to run the dynamic analysis.

The basic mechanism of the system consists of the interaction between a permanent magnet array and a rotating copper track mounted on an aluminum disk and put in motion by an electric motor. Such interaction causes lift and drag forces on the pad to be measured through the quasi-static test layout. Based on such measurements the dynamic test layout is set and the needed damping coefficient is tuned through a voice coil.

The mainframe of the system is designed as shown in the picture.

It features a supporting structure made of boxed steel, within which the electric motor is housed. The latter is connected to the disk through a torsional joint and a rotating shaft that transmits the motion to the disk. The shaft is fixed to the structure through two single row angular contact bearings housed in two designated flanges.



The rotating disk with the copper track mounted on top of it is contained in a shell made of two square aluminum plates and four aluminum columns. The walls are made of lexan, guaranteeing safety during experiment monitoring.

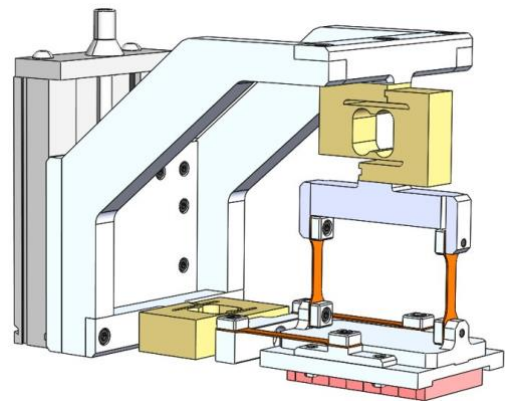
All of the components, except for the commercial ones, have been designed specifically for this experiment, all the design specifics are rigorously described in a designated section in the thesis.

The disk was subjected to both static and modal analysis to evaluate the potential criticalities, resulting in satisfactory behavior. The static deflection of the disk is small enough not to affect the experiment performance, while its resonance frequencies are high enough not to interfere with the system dynamics to be evaluated.

The shell containing the disk subsystem was subjected to modal analysis and also in this case the results are satisfactory since its resonance frequencies are much higher than the working frequency of this part of the system.

The layout designed to perform the quasi-static analysis is shown in the picture.

It features two load cells aimed at evaluating respectively the lift and drag forces acting on the system due to the interaction between the magnetic pad and the rotating copper track. A micrometric linear stage is implemented on the system to be tuned to impose the initial airgap between the pad and the runway. Two couples of vertical and horizontal flexure hinges connect the structure supporting the pad to the fixed part of the system, guaranteeing respectively longitudinal and vertical displacements. Numerous stators with different purposes are designed to connect and support every component of the measurement systems.



In particular, the two stators supporting the load cells and the two branches sustaining the upper load cell were subjected to linear static analysis. The results for all these components were satisfactory since the displacements due to the lift and drag forces were low enough not to affect the measurements, while the stress values to which the components are subject due to said forces are significantly low when compared to the yielding threshold of the material they are made of.

The whole assembly was subjected to modal analysis and the obtained results are satisfying since the resonance frequencies associated with every modal shape of the system are sufficiently higher than its working frequency.

An accurate description of the design specifics of every component of the system and thorough discussion about all the performed analyses are provided in a dedicated section on the thesis.

The quasi-static test layout has been assembled and a proper jig has been designed to guarantee the right placement of the magnets in their housing.

The quasi-static measurement procedure consists in fixing a certain initial airgap through the linear stage, driving the disk at the desired rotational speed and measuring the resulting lift and drag forces through the load cells. The measurement is iterated with varying values of the initial airgap.

The layout designed to perform the dynamic analysis is shown in the picture.

The magnetic pad and the micrometric linear stage are the same used for the quasi-static analysis. In addition it features a voice coil with the double purpose of balancing the weight of the sprung mass and providing a variable resistance to produce the needed damping. A sprung mass is suspended through two layers of four curved leaf springs each, while a similar configuration connects the unsprung mass (pad + support) to the stator rigidly fixed to the linear stage.

The system was subjected to modal analysis resulting in satisfactory values of the resonance frequency associated with the respective modal shapes.

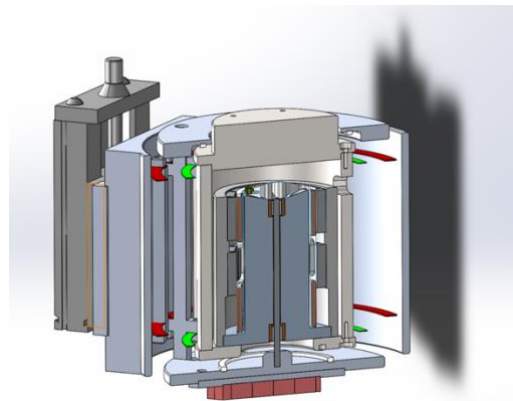
Further details about the design of the manufactured components of the system and on the modal analysis performance and results are provided in dedicated sections on the thesis.

The dynamic measurement procedure consists in fixing an initial airgap between the magnetic pad and the copper runway, driving the disk at the desired rotational speed and evaluating the damping of the system when changing the damping coefficient. Both the evaluation and the damping tuning are performed through the electrical parameters of the voice coil.

The control strategy to be implemented for the electric motor consists of a 3 phased driver performing speed control through both current and rotational speed feedbacks.

A possible control strategy to be implemented for the voice coil is based on current feedback with zero regulation of the static deformation of the elastic connections. Such deformation is detected through specific sensors placed on both the unsprung and the sprung masses.

The next steps to be tackled consist in assembling the remaining parts of the system, implementing the above-mentioned control strategies and performing the discussed measurements, which results will be the basis for further developments of the research in this field.



Aknlowledgements

*To my family,
the compass always pointing home.
To Amleto, the North;
to Margherita, the South;
to Fabrizia, the East;
and to me, the West.*

It is my pleasure to express my gratitude to Professor Andrea Tonoli, for being a dedicated and passionate teacher and to Professor Andrea Amati, along with Professor Tonoli himself, for giving me the opportunity to contribute to a project this ambitious and stimulating. Moreover, I would like to thank Dr. Bonfitto for being my reference in this journey and guiding me towards the finish line, and to my friend and colleague Federica Fanigliulo, for sharing both success and trouble and, most importantly, the enthusiasm for this work. A special mention goes to Dr. Torbjorn Lembke, from Hyperloop Transportation Technologies, for the trust he put in our team and the warmth with which he greets our progress. Finally, I wish to thank, from the bottom of my heart, my family and friends, for being my fuel all along this path and supporting every step I took on it. Your pride is my motivation and your joy is my success.

Table of Contents

<i>List of Tables</i>	<i>vii</i>
<i>List of Figures</i>	<i>viii</i>
<i>Introduction</i>	<i>1</i>
The Hyperloop Concept	1
State-of-the-art Analysis	4
Thesis Outline and Goals	5
<i>Test Bench – The Main Frame</i>	<i>6</i>
Design Overview	6
Relative Orientation	7
Main Frame Layout	8
Disk, Static Deflection and Modal Analysis	13
Static Deflection Analysis	13
Modal Analysis	17
Rotating System Shell, Frequency Analysis	20
Chapter 3	25
<i>Test Bench – The Quasi-Static Analysis</i>	<i>25</i>
Quasi-Static Test Layout	25
Stators, Static Deflection	33
Quasi-Static Test Layout, Modal Analysis	38
Quasi-Static Test Layout, Assembling	43
<i>Test Bench – The Dynamic Analysis</i>	<i>46</i>
Dynamic Test Layout, Design Procedure	46
Dynamic Test Layout	53
Dynamic Test Layout, Modal Analysis	59
<i>Next Steps, Conclusions and Further Developments</i>	<i>64</i>
Control Strategies	64
Measurement Procedures	66
Conclusions	67
<i>Bibliography</i>	<i>69</i>

List of Tables

Table 2.1 – SKF Bearings Dimensions	9
Table 2.2 – SKF Bearings Calculation Data	10
Table 2.3 – Kollmorgen Motor Data	12
Table 2.4 – RW Torsional Joint Data	13
Table 3.1 – Norelem Linear Stage Data	27
Table 3.2 – HBM Force Transducer Data	28
Table 4.1 – Comparison Between the Desired Force and the Voice Coil Output	54
Table 4.1 – Geeplus Voice Coil Behavior	59
Table 4.2 – Geeplus Voice Coil Data	59

List of Figures

Figure 1.1 – May 23, 2019 - China's first high-speed maglev train testing prototype in Qingdao	2
Figure 1.2 – Hyperloop Alpha, qualitative drawing	3
Figure 1.3 – Hyperloop Alpha, qualitative drawing	3
Figure 2.1 – Axial symmetry layout	7
Figure 2.2 – Radial symmetry layout	7
Figure 2.3 – Test rig main frame: section view	8
Figure 2.4 – SKF Bearing, Drawings	9
Figure 2.5 – Boxed steel section	11
Figure 2.6 – Kollmorgen Motor, Drawings	11
Figure 2.7 – RW Torsional Joint, Drawings	12
Figure 2.8 – Disk, Linear Static Analysis, constraints	14
Figure 2.9 – Disk, Linear Static Analysis, load	15
Figure 2.10 – Disk, Linear Static Analysis, mesh	15
Figure 2.11 – Disk, Linear Static Analysis, results	16
Figure 2.12 – Disk + Flange, Linear Static Analysis, conditions	16
Figure 2.13 – Disk + Flange, Linear Static Analysis, mesh	17
Figure 2.14 – Disk + Flange, Linear Static Analysis, results	17
Figure 2.15 – Disk + Flange, Frequency Analysis, Natural Mode 1	18
Figure 2.16 – Disk + Flange, Frequency Analysis, Natural Mode 2	18
Figure 2.17 – Disk + Flange, Frequency Analysis, Natural Mode 3	18
Figure 2.18 – Disk + Flange, Frequency Analysis, Natural Mode 4	19
Figure 2.19 – Disk + Flange, Frequency Analysis, Natural Mode 5	19
Figure 2.20 – Disk + Flange, Frequency Analysis, Further Natural Modes	20
Figure 2.21 – Main Frame, Frequency Analysis, Mesh	21
Figure 2.22 – Main Frame, Frequency Analysis, Natural Mode 7, Resulting Amplitude Legend	22
Figure 2.23 – Main Frame, Frequency Analysis, Natural Mode 8	22
Figure 2.24 – Main Frame, Frequency Analysis, Natural Mode 9	22
Figure 2.25 – Main Frame, Frequency Analysis, Natural Mode 10	23
Figure 2.26 – Main Frame, Frequency Analysis, Natural Mode 11	23
Figure 2.27 – Main Frame, Frequency Analysis, Natural Mode 12	24
Figure 3.1 – Quasi-Static Test Layout, 3D Model	26
Figure 3.2 – Norelem Linear Stage, Drawings	27
Figure 3.3 – HBM Force Transducer, Drawings	28
Figure 3.4 – Quasi-Static Test Layout, Vertical Springs Design	29
Figure 3.5 – Magnets Arrangement	29
Figure 3.6 – Quasi-Static Test Layout, Horizontal Springs Design	30
Figure 3.7 – Quasi-Static Test Layout, Stator 7. Design	31
Figure 3.8 – Quasi-Static Test Layout, Stator 8. Design	32
Figure 3.9 – PM Pad Housing, Upper and Lower Components	32
Figure 3.10 – Quasi-Static Test Layout, Stator 11., Linear Static Analysis, Conditions	34

Figure 3.11 – Quasi-Static Test Layout, Stator 11., Linear Static Analysis, Mesh	34
Figure 3.12 – Quasi-Static Test Layout, Stator 11., Linear Static Analysis, Results	34
Figure 3.13 – Quasi-Static Test Layout, Stator 10., Linear Static Analysis, Conditions	35
Figure 3.14 – Quasi-Static Test Layout, Stator 10., Linear Static Analysis, Mesh	35
Figure 3.15 – Quasi-Static Test Layout, Stator 10., Linear Static Analysis, Results	36
Figure 3.16 – Quasi-Static Test Layout, Stator 8., Linear Static Analysis, Conditions	37
Figure 3.17 – Quasi-Static Test Layout, Stator 8., Linear Static Analysis, Mesh	37
Figure 3.18 – Quasi-Static Test Layout, Stator 8., Linear Static Analysis, Results	38
Figure 3.19 – Quasi-Static Test Layout, Frequency Analysis, Constraints	39
Figure 3.20 – Quasi-Static Test Layout, Frequency Analysis, Mesh	39
Figure 3.21 – Quasi-Static Test Layout, Frequency Analysis, Natural Mode 1	40
Figure 3.22 – Quasi-Static Test Layout, Frequency Analysis, Natural Mode 2	40
Figure 3.23 – Quasi-Static Test Layout, Frequency Analysis, Natural Mode 3	41
Figure 3.24 – Quasi-Static Test Layout, Frequency Analysis, Natural Mode 4	41
Figure 3.25 – Quasi-Static Test Layout, Frequency Analysis, Further Natural Modes	42
Figure 3.26 – Quasi-Static Test Layout, Assembling	43
Figure 3.27 – Quasi-Static Test Layout, Assembling	43
Figure 3.28 – Magnetic Pad Jig, Element 1	44
Figure 3.29 – Magnetic Pad Jig, Element 2	44
Figure 3.30 – Quasi-Static Test Layout, Jig Implementation	45
Figure 4.1 – Dynamic Test Layout, 2D Model	47
Figure 4.2 – Dynamic Test Layout, 3D Model	47
Figure 4.3 – Dynamic Test Layout, 3D Model	48
Figure 4.4 – Dynamic Test Layout, 3D Model	49
Figure 4.5 – Dynamic Test Layout, 3D Model	50
Figure 4.6 – Dynamic Test Layout, 3D Model	50
Figure 4.7 – Dynamic Test Layout, 3D Model	51
Figure 4.8 – Dynamic Test Layout, 3D Model	52
Figure 4.9 – Dynamic Test Layout, Final Configuration, 3D Model	53
Figure 4.10 – Dynamic Test Layout, Stator 3. Design	55
Figure 4.11 – Dynamic Test Layout, Stator 4. Design	56
Figure 4.12 – Dynamic Test Layout, Element 5. Design	57
Figure 4.13 – Dynamic Test Layout, Element 6. Design	57
Figure 4.14 – Geeplus Voice Coil, Drawings	58
Figure 4.15 – Dynamic Test Layout, Frequency Analysis, Constraints	60
Figure 4.16 – Dynamic Test Layout, Frequency Analysis, Mesh	61
Figure 4.17 – Dynamic Test Layout, Frequency Analysis, Natural Mode 1	61
Figure 4.18 – Dynamic Test Layout, Frequency Analysis, Natural Mode 2	62
Figure 4.19 – Dynamic Test Layout, Frequency Analysis, Natural Modes 3 and 4	62

Figure 4.20 – Dynamic Test Layout, Frequency Analysis, Natural Modes 5 and 6	63
Figure 4.21 – Dynamic Test Layout, Frequency Analysis, Natural Modes 7 and 8	63
Figure 4.22 – Dynamic Test Layout, Frequency Analysis, Natural Modes 9 and 10	63
Figure 5.1 – Electric Motor Control Strategy	64
Figure 5.2 – Electric Motor Control Strategy	65
Figure 5.3 – Voice Coil Control Strategy	65
Figure 5.4 – Lift and Drag Forces Simulation Results	66
Figure 5.5 – Selection of the Optimal Damping Value	67

Chapter 1

Introduction

The purpose of this work is to describe in detail every step of the procedure of designing a test bench aimed at simulating and studying the behavior of a levitation system working in line with Hyperloop Transportation Technologies' guidelines.

The project is being developed in cooperation between Hyperloop itself and a team from Politecnico di Torino, which includes professors, researchers, PhD students and Master's grad students, based in the Mechatronic's lab in PoliTo.

In this chapter a brief description of the Hyperloop Technology and the framework in which it is being developed will be provided, along with a literature analysis and an outline of the thesis work itself.

The Hyperloop Concept

The climate crisis is becoming more of a compelling issue every day and the transport industry is one of the main actors in this scenario, accounting for nearly one-third of the yearly global emissions of CO₂ [1]. State administrations all over the world are working in the direction of reducing the environmental impact of this field, through incentives and funding specifically aimed at the research and development of more sustainable technologies. The goal is to combine the need for an increasingly efficient transportation network with the one for a significant decrease of the emissions coming from this sector.

In this context, one of the most promising technologies in course of development consists in magnetically levitated (maglev) trains, which represent an improvement in numerous ways.

Classic wheeled trains can reach limited speeds, these limits being imposed by the wheels themselves: the friction between the wheels and the railway causes wear and tear and minor imperfections on the wheel can magnify into intense vibrations. Even while traveling at these limited speeds, the maintenance costs are significant [2].

Maglev trains, on the other hand, travel suspended at a short distance from a guide track, by means of a magnetic field, which also serves as the only source of propulsion [3], making this a potentially zero emissions technology. Additionally, as a consequence, the only friction the train encounters is caused by the wind, which allows a maximum speed limit nearing 600 km/h.



Figure 1.1 - May 23, 2019 - China's first high-speed maglev train testing prototype in Qingdao [4]

Unfortunately, this technology didn't find the expected market worldwide because, when compared with air travel, under the same conditions of distance to cover, the difference in terms of time taken is negligible with respect to the significant increase of the costs.

In this framework, the Hyperloop project represented a breakthrough, since it introduced the concept of traveling in low-pressured tubes, in other words a vacuum-sealed environment, which allows the train to reach considerably higher speeds, reducing to nearly zero the air resistance and friction obstacles of high-speed travel [2].

The modern Hyperloop concept, the Hyperloop Alpha, was proposed in 2013 by SpaceX as an open-source design, so that it would be available for anyone to further develop, and it consisted of sealed and pressurized capsules, levitated through air bearings and propelled by a linear induction motor and axial compressors, in order to avoid any mechanical contact [5].

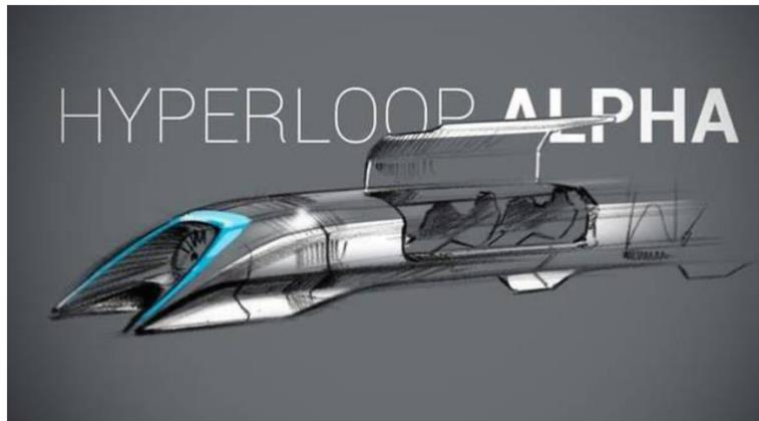


Figure 1.2 - Hyperloop Alpha, qualitative drawing [6]

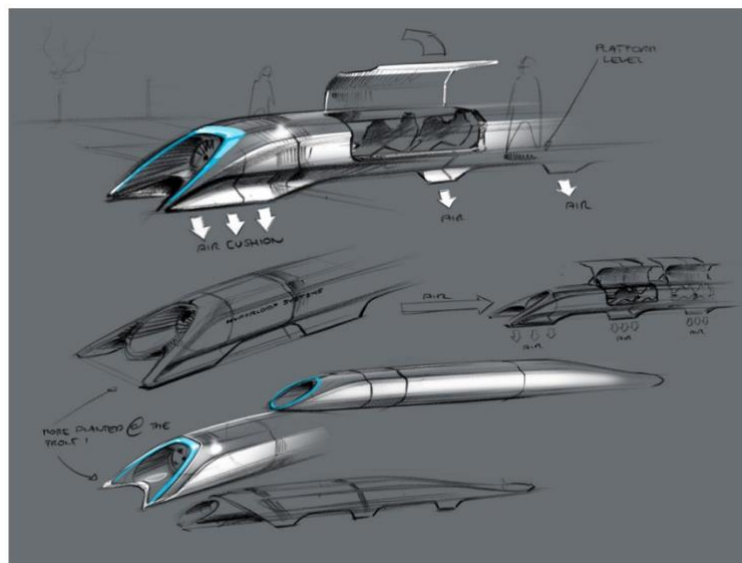


Figure 1.3 - Hyperloop Alpha, qualitative drawing [6]

In a later stage, the air bearings were replaced by magnetic pads, following the Inductrack concept [7]. The system is based on the principle of electrodynamic levitation: every capsule features permanent magnets (henceforth PM) that cause a magnetic field on the guide track and consequently eddy currents, following Faraday-Lenz law. The currents exert both lift and drag force components on the capsule, the lift force acts in the vertical direction while the drag force acts in the propulsion direction but with opposite orientation, thus behaving like a friction factor, owing to the fact that it is caused by the reluctance of the circuit.

In this context, the lift-to-drag ratio increases with speed, making this one of the most suitable technologies for ultra-high-speed applications.

State-of-the-art Analysis

The idea of the electrodynamic levitation principle applied to the transportation environment, and in particular the Hyperloop concept, has attracted the interest of several, resulting in a consistent number of researches and experimental validations being carried out in recent years. Below, a synthetic analysis of the state of the art through literature and feasibility studies will be conducted.

The aerodynamic behavior of the pod was extendedly analyzed, among the others, by Nick and Sato [8] who describe the results of three-dimensional compressible flow simulation they have performed in order to predict the transition from laminar to turbulent flow.

In the context of propulsion, Choi, Lee and Jo [9] propose a system based on sub-sonic linear synchronous motors (LSMs) with high-temperature superconducting magnets, aimed at accelerating to a velocity of 1200 km/h in the near-vacuum tubes of 0.001 atm in which the Hyperloop is set to travel; Tudor and Paolone [10], on the other hand, introduce a sizing method meant to minimize the total number of battery cells that supply the capsule's propulsion while maximizing its performance.

Another subject, nucleus of several works, is the idea to start from the concept of electrodynamic bearings (EDBs), extensively described by Post and Ruytov [7] and used for rotating machines, and readapt it in a translational variant, in order to implement stable passive levitation in the system. This is the core of the work of Tonoli et al. [11-13], along with Lembke [14, 15] and Filatov and Maslen [16], in the works of whom the intrinsic unstable nature of EDBs has been identified and stabilized through different techniques, and different configurations of EDBs were modeled and experimented.

The levitation aspect is also tackled by the research efforts of Chaidez, Bhattacharyya and Karpets [17] and Guo et al. [18], the latter proposing a null-flux coil electrodynamic suspension structure to provide a high lift-to-drag ratio.

Another interesting point of view is the one of Galluzzi et al. [19] and Circosta et al. [20], who propose a multi-domain approach to the stabilization of the electrodynamic levitation system, describing the behavior of the system when coupled with mechanical domain variables. Galluzzi proposes a lumped-parameter model with a multiple-branch circuit, tuned through finite-elements simulations to replicate the electrodynamic behavior, along with linearization and analysis of the multi-domain equations and a discussion on the unstable nature of the

system. Circosta, on the other hand, introduces the concept of a secondary suspension aimed at stabilizing the system, designed through the optimization of stability and dynamic performances.

Given the significant appeal this technology exerts, several feasibility studies have been carried out in different environments. An implementation that draws particular attention is the one conducted by General Atomics in collaboration with the Federal Transit Administration [21], consisting of a 120m long maglev test track, built in California. The system under test presents permanent magnets tied to the cart, which is propelled by a linear induction motor, resulting in a Hyperloop-like context, except for the absence of a vacuum-sealed environment. As explained before, the interaction between the magnets and the guide track causes the levitation and guidance of the system. Tests on system dynamics and journey quality were performed on this environment resulting in more than satisfactory data in terms of lift-to-drag ratio and lift-off velocity, while airgap data both in levitation and guidance were higher than expected, even if bounded with auxiliary wheels to mask the unstable behavior of the levitation system.

Thesis Outline and Goals

In the wake of the previously discussed researches and studies, the Politecnico di Torino, in cooperation with Hyperloop Transportation Technologies, has developed a project for a test bench designed to reenact the dynamic behavior of a Hyperloop system, in order to study and correct its instability by implementing the multi-domain approach described in the research work by Galluzzi et al. [17]. The purpose of this work is to describe every step of the procedure of designing such a bench, in particular the design and testing phases carried out through the CAD environment of SolidWorks.

In the following chapters the design of different aspects of the test rig will be dealt with: firstly, the design of the main frame of the system will be tackled, describing the components and discussing the results given by the frequency analysis. The following two chapters will cover the topic of the design procedure of the two layouts arranged to perform the quasi-static analysis and the dynamic analysis of the system, each of the two will be provided with a procedure description and results analysis of the respective virtual tests and simulations. The specifics of both the systems will be highlighted and motivated.

Finally, conclusions will be drawn and further developments of the project will be discussed.

Chapter 2

Test Bench – The Main Frame

In this chapter, the design and functionalities of the main frame of the system will be discussed and design choices will be motivated. The main components will be identified and virtual test procedures carried out on the system will be described, along with a results analysis.

Design Overview

The experiment aims at simulating and validating the results of the studies previously described in the state-of-the art analysis, and in particular the multi-domain approach.

A significant part of the above mentioned method consists in evaluating lift and drag forces, along with the stability conditions, in order to do so two requirements are needed: the system must be able to perform vertical displacement, and relative longitudinal speed between the capsule model and the track must be guaranteed.

The track has been designed to be circular considering that the simulation must be carried out on a laboratory scale and a linear runway, although being more straightforward, would have been excessively long, to run experiments for the time sufficient to evaluate all the variables. As a result, the track has been designed as a circular crown of diameter D , mounted on a circular plate of diameter D' , rotating by means of an electric motor.

The superior part of the bench consists of a mass m and the damping system (yet to be discussed), modelling the whole capsule, connected to a PM array which interacts with the track.

The length L of the PM array is defined such that the D/L ratio is high enough to approximate the direction of the tangential velocity vector v as constant along the entire pad length.

Relative Orientation

Different configurations are possible in terms of disk and track relative positioning, two in particular are interesting as they exploit either axial or radial symmetry.

A qualitative representation of both the arrangements is provided in the following pictures.

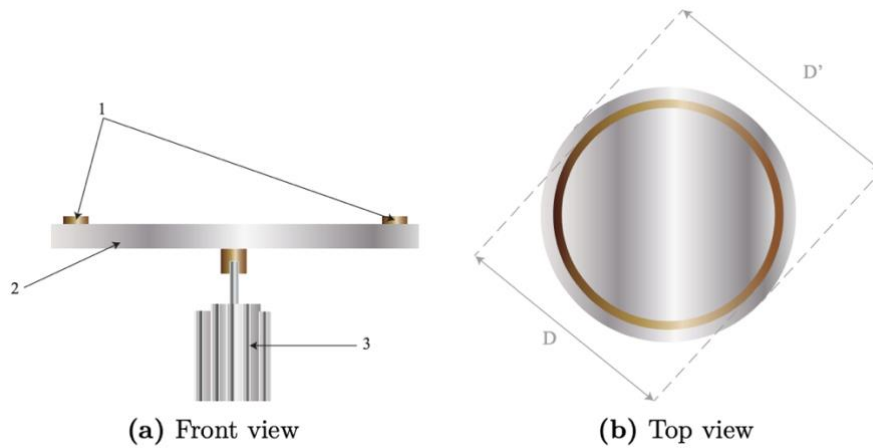


Figure 2.1 - Axial symmetry layout. 1) Track; 2) Rotating disk; 3) Motor.
Courtesy of Fanigliulo, F.

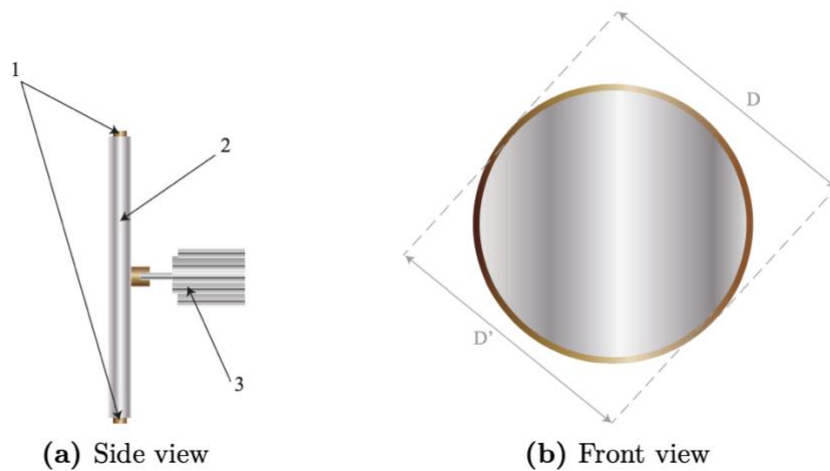


Figure 2.2 - Radial symmetry layout. 1) Track; 2) Rotating disk; 3) Motor.
Courtesy of Fanigliulo, F.

On the other hand, in the radial symmetry layout, the track curvature makes the interaction with the PM array more complex. The issue can be solved either by raising the D/L ratio, increasing the dimensions of the bench as well, or by adopting curved magnets for the array.

Main Frame Layout

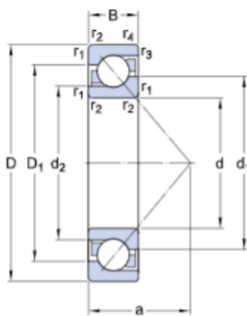
[illegible]

8

The steel and lexan structure surrounding the disk serves both the functions of supporting the measurement system and guaranteeing safety during experiment monitoring. A torsional joint and a shaft connect the disk to the electric motor used for propulsion and two contact bearings support the shaft and prevent the motion of the rotational axis.

In the upcoming section all the components of the main frame of the system will be described, following the order imposed by the call-out balloons.

1. Two square aluminum plates, with side equal to 1300 mm and thickness equal to 25 mm, delimit the working area up and down, the upper plate is provided with a hole in correspondence of the position of the upper part of the bench, in which the system will be inserted.
2. Two bearings serve the function of supporting the shaft guaranteeing its rotational motion. The selected model is the SKF 7206 BECBP [23], a single row angular contact bearing with the following characteristics:



DIMENSIONS

d	30 mm	Bore diameter
D	62 mm	Outside diameter
B	16 mm	Width
d1	≈42.65 mm	Shoulder diameter inner ring (large side face)
d2	≈36.13 mm	Shoulder diameter inner ring (small side face)
D1	≈50.1 mm	Shoulder diameter outer ring (large side face)
a	27.3 mm	Distance pressure point
r1,2	min.1 mm	Chamfer dimension
r3,4	min.0.6 mm	Chamfer dimension outer ring small side face

Figure 2.4 - SKF Bearings

Table 2.1 – SKF Bearings Dimensions

CALCULATION DATA

Basic dynamic load rating	C	24 kN
Basic static load rating	C_0	15.6 kN
Fatigue load limit	P_u	0.655 kN
Reference speed		13 000 r/min
Limiting speed		14 000 r/min
Calculation factor	A	0.004
Calculation factor	k_r	0.095
Calculation factor	e	1.14

Table 2.2 – SKF Bearings Calculation Data

3. The rotational shaft transfers the motion from the motor to the disk, hence the cylindrical geometry of its section with a diameter of 150 mm and a length of 300 mm. This component is made of Steel.
4. Two steel flanges, embedded in the two aluminum plates, act as housing for the two previously described bearings. They have a diameter of 240 mm and a width of 53 mm. The material chosen for these components is the S355J2H steel.
5. Four lexan plates are needed for a support function for the structure, moreover they represent a safety device that also allows monitoring the course of the experiment. They are designed with a length of 1030mm, a width of 190 mm and a thickness of 10 mm.
6. The track is made of copper, material chosen for its propensity to react with the magnets, and has an external diameter of 1000 mm and an internal diameter of 880 mm.
7. The disk is made of carbon steel and it has a diameter of 1100 mm and a thickness of 20 mm. It is framed on specific support on the rotational shaft.
8. 24 reinforcements are placed on every angle between two adjacent beams constituting the supporting structure. They have a triangular shape, with two orthogonal sides which measure 100 mm and a thickness of 3 mm. The material chosen for these components is S355J2H steel.

9. Eight horizontal beams are placed on two layers to reinforce the legs of the supporting structure. They are made of boxed S355J2H steel and they have a length of 1180 mm. The section is represented and dimensioned in the following picture.

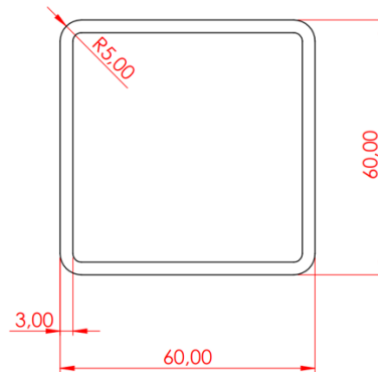


Figure 2.5 - Boxed steel section

10. The electric motor represents the propulsion source of the system. The chosen model is the Kollmorgen AKM74L [24] which characteristics are described in the following table.

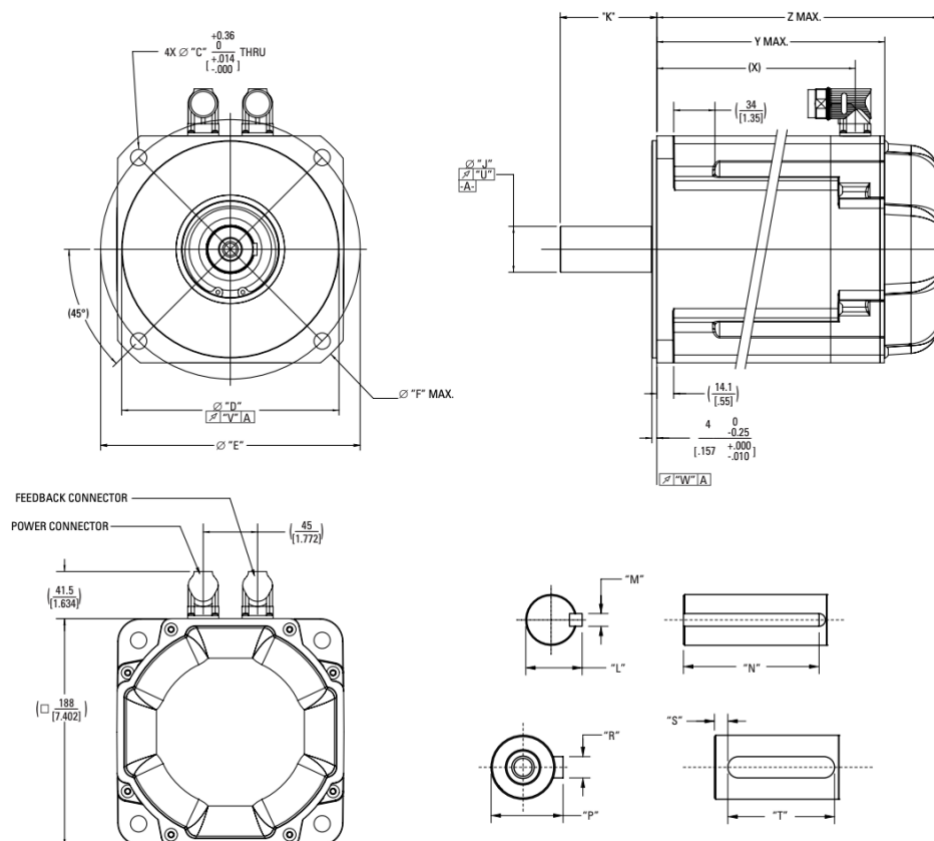


Figure 2.6 – Kollmorgen Motor, Drawings

Maximum power	5.47 kW
Rated torque	49.7 Nm
Rated speed	1200 rpm

Table 2.3 – Kollmorgen Motor Data

11. Four vertical beams constitute the legs of the supporting structure. They are made of the same boxed steel as the horizontal ones (9.) with the same section, but they have a length of 550 mm.
12. A torsional joint is needed to link the electric motor to the rotational shaft. The chosen model is the RW Italia BK2-500-169 [25], which features a bellow in high flexibility stainless steel and a steel clamp. Design specifics are described in the following table.

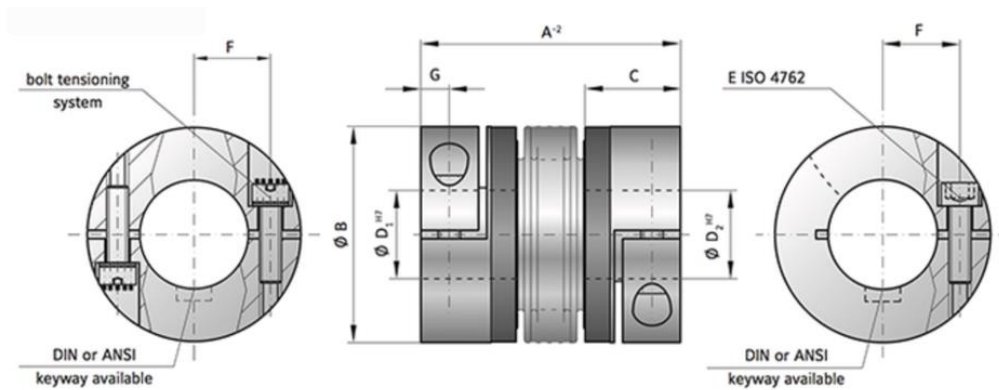


Figure 2.7 - RW Torsional Joint, Drawings




BK2 Series		500
Rated torque (Nm)	T_{KN}	500
Overall length (mm)	A^{-2}	133 146 169
Fit length (mm)	C	51
Inside diameter possible from \varnothing to \varnothing H7 (mm)	D_1/D_2	35-60
Outside diameter (mm)	B	124
Moment of inertia (10^{-3} kgm^2)	$J_{ges.}$	14,3 14,6 14,8
Approximate weight (kg)		6,3
Torsional stiffness (10^3 Nm/rad)	C_T	510 500 400
Axial \pm  (mm))	max.	2,5 3,5 4,5
Lateral \pm  (mm)	max.	0,3 0,35 1
Angular \pm  (degree)	max.	1 1,5 2
Axial spring stiffness (N/mm)	C_a	70 48 85
Lateral spring stiffness (N/mm)	C_r	2500 840 614
Fastening screw (ISO 4762)	E	M16
Tightening torque of the fastening screw (Nm)	E	200
Distance between centerlines (mm)	F	41
Distance (mm)	G	16,5
Hub material		Steel optional Aluminium
		500

Table 2.4 – RW Torsional Joint Data

Disk, Static Deflection and Modal Analysis

Before getting into production, the system needs to be submitted to virtual testing in order to assess its feasibility and the safety of the working conditions.

Static Deflection Analysis

When a body is subject to an applied load, the body itself tends to deform and the effect of the load is transmitted throughout the body. Internal forces and reaction are induced by the external load because the body tends to render to a state of equilibrium. In the case in question the body is represented by the disk, and the external load is represented by the dynamic measuring system with its 22 kg weight.

A test is needed to ensure that the external load causes a deformation small enough not to influence the performance of the experiment. Such a test is called a Linear Static Analysis.

A proper tool is provided by the SolidWorks environment to perform such simulation to calculate displacements, strains, stresses and reaction forces under the effect of applied loads [26].

In order to perform said simulation some parameters need to be set, firstly, the right material must be associated to the piece or assembly to analyze, then the constraints must be applied to guarantee a behavior of the system which is as similar as possible to the real one, the load must be tuned and applied in the right position and finally a mesh must be generated on the design.

In order to simulate the behavior of the disk when subject to the load of the upper part of the bench, the test was carried out with two different configurations.

In the first configuration, the disk alone is taken into consideration, the associated material is carbon steel, with an elastic modulus of $2.1 \times 10^{11} \text{ N/m}^2$ and a density mass coefficient equal to 7800 kg/m^3 .

The constraint chosen is a fixed geometry restraint applied on the lower surface of the disk, on the subsection of the surface that, in the real environment, is in contact with the flange, where the constraint occurs.

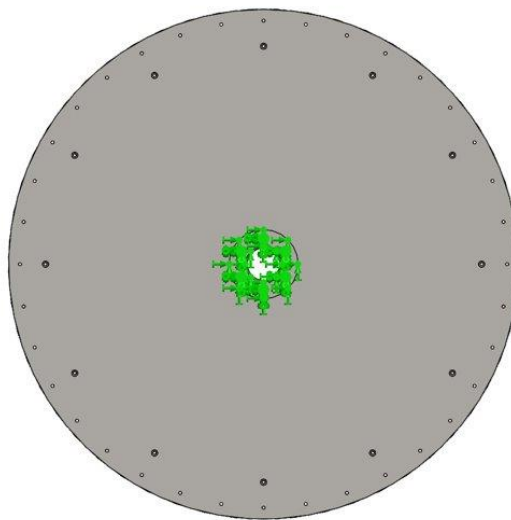


Figure 2.8 – Disk, Linear Static Analysis, constraints

The load, equal to 215 N, is applied on the portion of the disk corresponding to the position of the pad. This configuration represents the worst possible situation the system could face, in which the whole dynamic measurement subsystem is resting on the disk. It is chosen not to apply the load on a single point in order to avoid mathematical discontinuities.

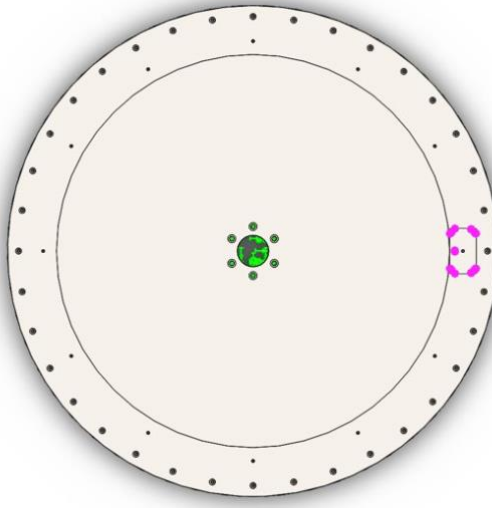


Figure 2.9 – Disk, Linear Static Analysis, load

Finally, the mesh is created. The mesh generates 3D tetrahedral solid elements, 2D triangular shell elements, and 1D beam elements in order to divide the model into small constituents of simpler shape, connected to each other at the common points [26]. The mesh configuration for this simulation appears as follows.

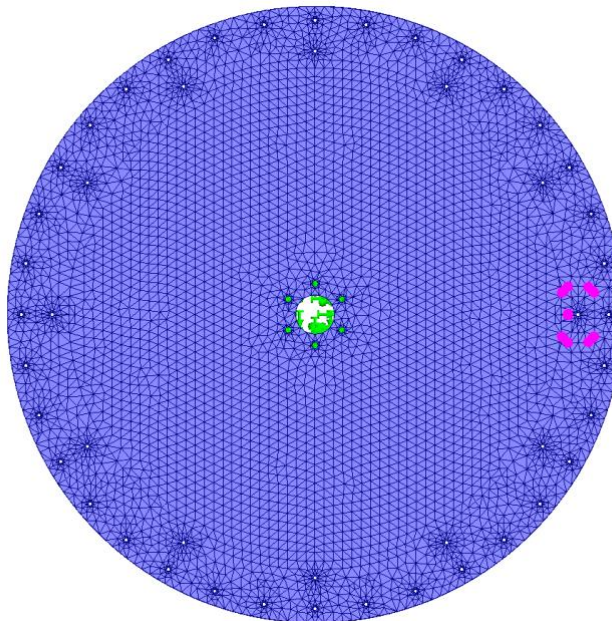


Figure 2.10 – Disk, Linear Static Analysis, mesh

Once these parameters are set, the simulation can be performed. The consequent deformation appears like in the following picture.

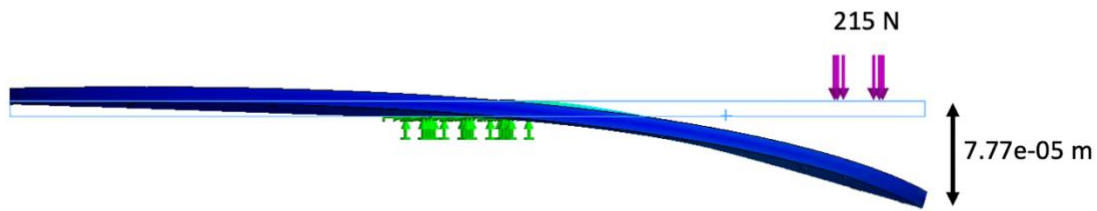


Figure 2.11 – Disk, Linear Static Analysis, results

The displacement caused by the load is equal to 7.77×10^{-5} m, which is considered a satisfying value.

In the second configuration the flange is taken into account along with the disk. The flange is assigned the same material as the disk.

In this case the restraints are applied on the flange itself, in correspondence with the position of the bearings, to simulate a similar behavior with respect to the real system. In this case, too, it is chosen to apply a fixed geometry restraint.

The load is applied in the same position as before.

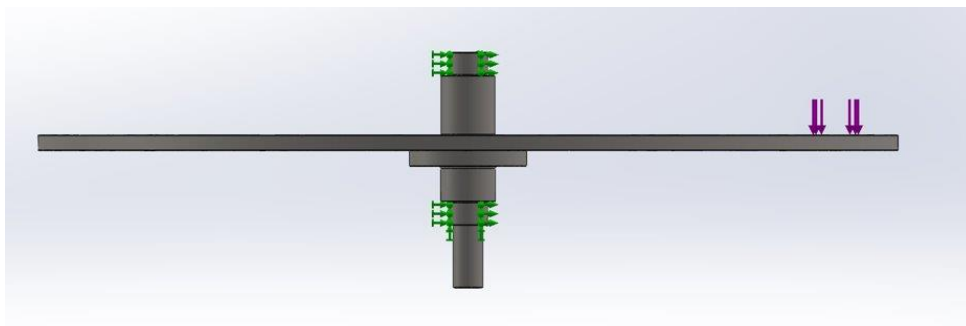


Figure 2.12 – Disk + Flange, Linear Static Analysis, conditions

The mesh is created and, as it can be noticed in the following figure, its density depends by the dimensions of the component.

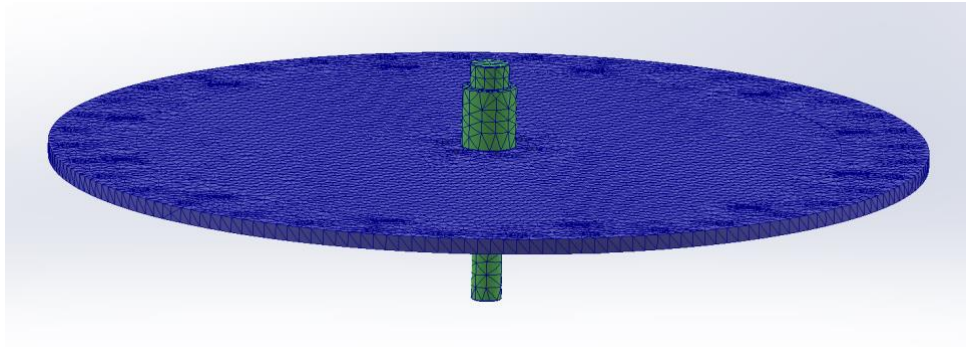


Figure 2.13 – Disk + Flange, Linear Static Analysis, mesh

Finally, the simulation can be performed. The resulting deformation is represented in the following picture.

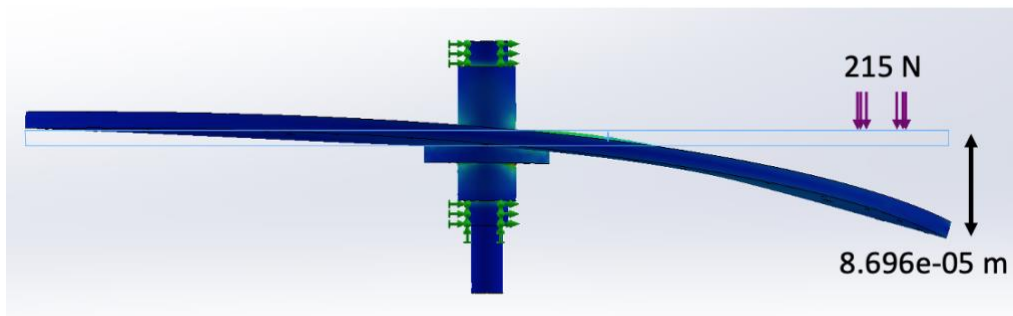


Figure 2.14 – Disk + Flange, Linear Static Analysis, results

With this layout, the displacement resulting from the simulation is equal to 8.696×10^{-5} m. This value is considered satisfactory, too.

Modal Analysis

The disk undergoes a procedure of modal analysis, too. The topic of this kind of test will be better covered in the next paragraph.

To perform this simulation a fixed geometry constraint is applied on the lower surface of the disk, in correspondence of the portion of surface that interacts with the flange in the real system, to guarantee that the simulation conditions are as similar as possible to the real working conditions. No loads are applied.

The modal analysis has the purpose of detecting the natural vibration modes of the system, to ensure that they don't interfere with the experiments to be performed. The results of such analysis are the following.

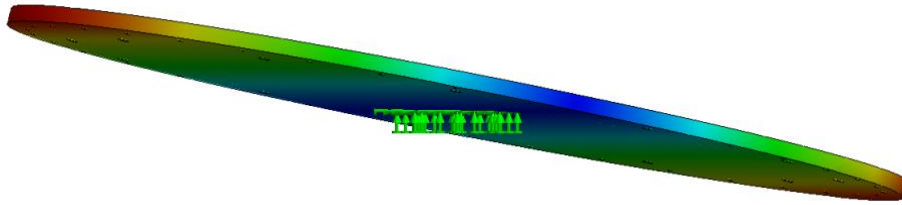


Figure 2.15 – Disk + Flange, Frequency Analysis, Natural Mode 1

The resonance frequency associated with this modal shape is 61.707 Hz.

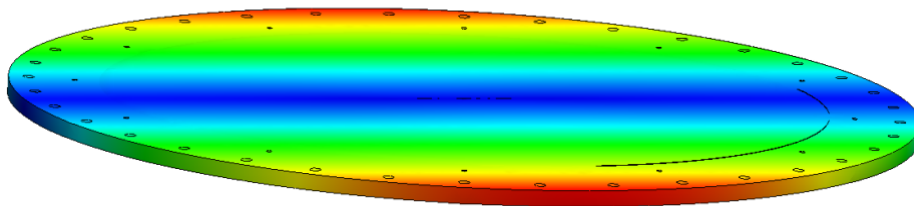


Figure 2.16 – Disk + Flange, Frequency Analysis, Natural Mode 2

The resonance frequency associated with this modal shape is 61.732 Hz.

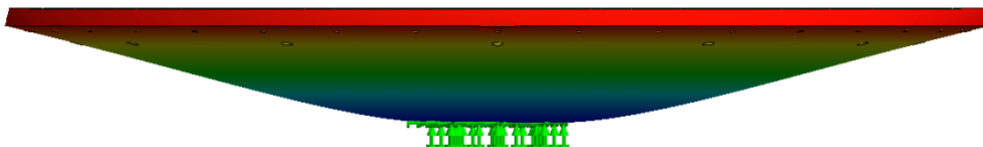


Figure 2.17 – Disk + Flange, Frequency Analysis, Natural Mode 3

The resonance frequency associated with this modal shape is 72.912 Hz.

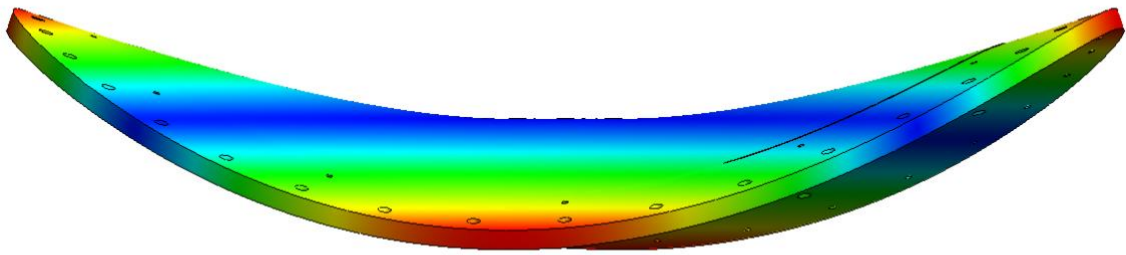


Figure 2.18 – Disk + Flange, Frequency Analysis, Natural Mode 4

The resonance frequency associated with this modal shape is 91.84 Hz.

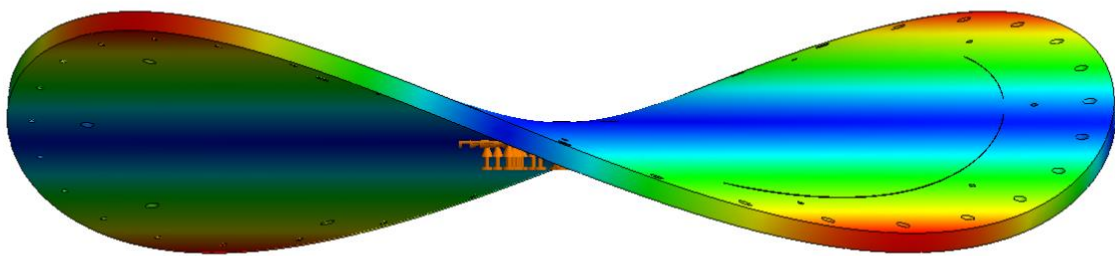


Figure 2.19 – Disk + Flange, Frequency Analysis, Natural Mode 5

The resonance frequency associated with this modal shape is 91.89 Hz.

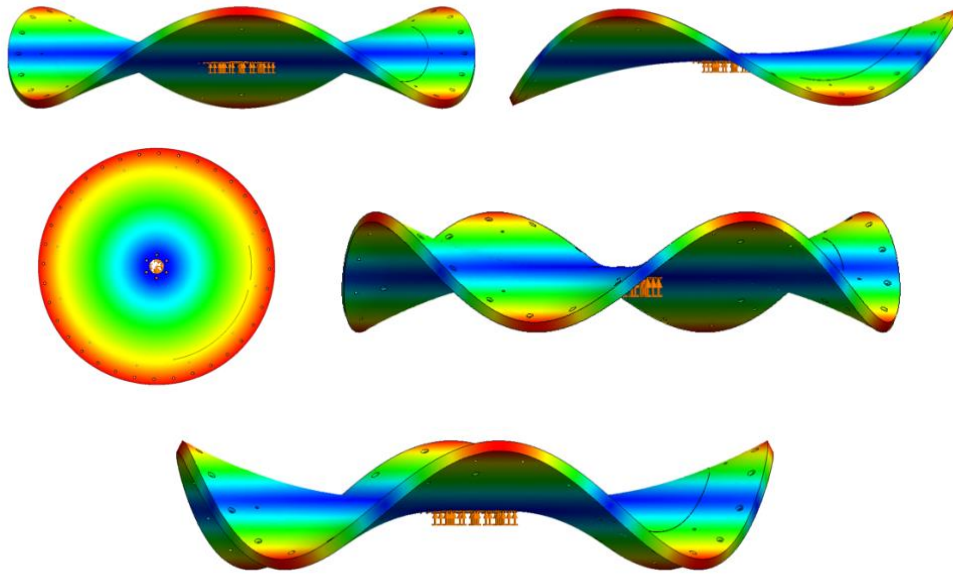


Figure 2.20 – Disk + Flange, Frequency Analysis, Further Natural Modes

The resonance frequencies associated with these modal shapes have higher order of magnitude hence are considered of little significance to the means of the experiment.

The working frequency of this system is 12.7 Hz ca. and all the resonance frequencies resulting from the analysis are significantly higher, consequently, is safe to say that the results are satisfying.

Rotating System Shell, Frequency Analysis

This section deals with another kind of simulation performed on a different part of the bench.

Every structure tends to vibrate at what is called its natural or resonance frequencies. Each of these resonant frequencies is associated a certain deformation of the system, resulting in a modal shape assumed by the system itself when it vibrates at the respective frequency.

It is crucial that each one of the resonance frequencies of the system is superior to its working frequency since, when the two coincide, the system undergoes large displacements and stress [26]. In the case in question, the working frequency is about 13 Hz.

As the system in question was designed to test a dynamic behavior, studies are needed to explore its resonance frequencies and its natural modes, to determine whether or not they can impact the results of the experiment. The SolidWorks environment provides a tool that allows

the designer to perform the frequency analysis of a single piece or a whole assembly, with the aim of studying its dynamic response.

Before performing such analysis some preliminary parameters must be set, the right material must be assigned to the corresponding pieces and the mesh must be created.

This analysis is carried out on the shell of the rotating system, which is composed of two square plates, four columns separating the upper and lower layers, two flanges and four transparent panels enclosing the system.

The material assigned to the two square plates, along with the four spacers and the cover of the upper flange, is the 6061 Aluminum Alloy, with elastic modulus equal to 6.9×10^{10} N/m² and mass density coefficient equal to 2700 kg/m³.

The material assigned to the two flanges is Carbon Steel, with elastic modulus equal to 2.1×10^{11} N/m² and mass density coefficient equal to 7800 kg/m³.

The material assigned to the transparent panels is rigid PVC, with elastic modulus equal to 2.41×10^9 N/m² and mass density coefficient equal to 1300 kg/m³.

Finally, the mesh is generated by the software based on global element size, tolerance and mesh control, the mesh control was tuned according to the requirements of every single component.

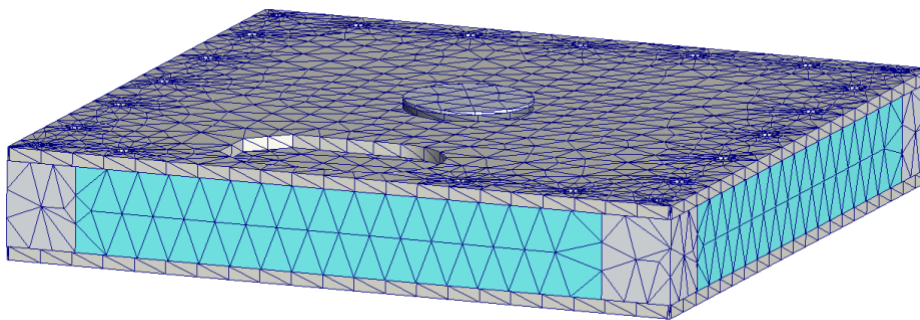


Figure 2.21 – Main Frame, Frequency Analysis, mesh

At this point the simulation can be performed.

The first 6 resonance frequencies are around 0 and don't provide any deformation to the system. Starting from the 7th, the resulting modal shapes are represented in the following pictures and the respective resonance frequencies are reported.

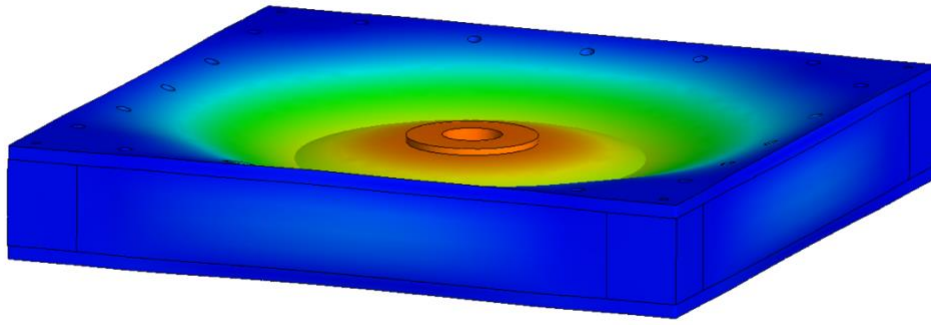


Figure 2.22 – Main Frame, Frequency Analysis, Natural mode 7

The resonance frequency associated with this modal shape is 88.676 Hz.

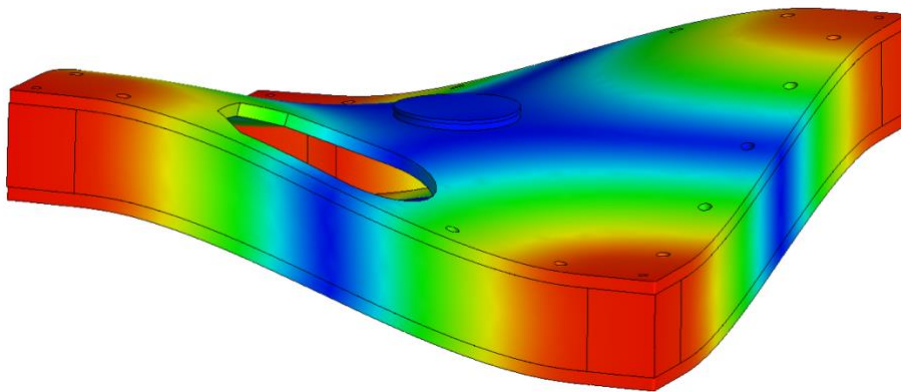


Figure 2.23 – Main Frame, Frequency Analysis, Natural Mode 8

The resonance frequency associated with this modal shape is 111.8 Hz.

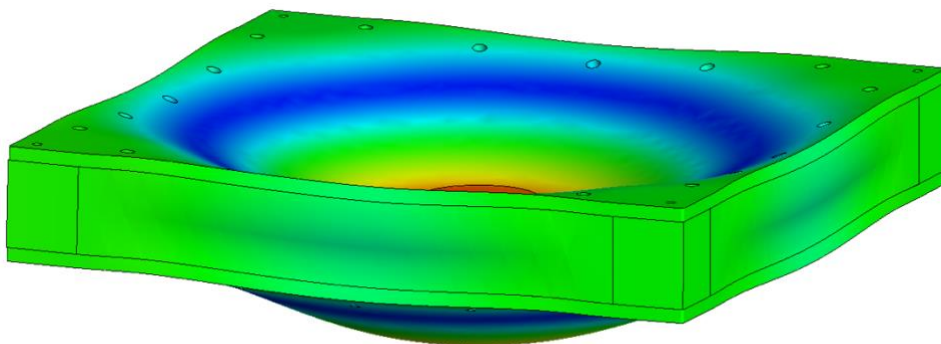


Figure 2.24– Main Frame, Frequency Analysis, Natural Mode 9

The resonance frequency associated with this modal shape is 121.78 Hz.

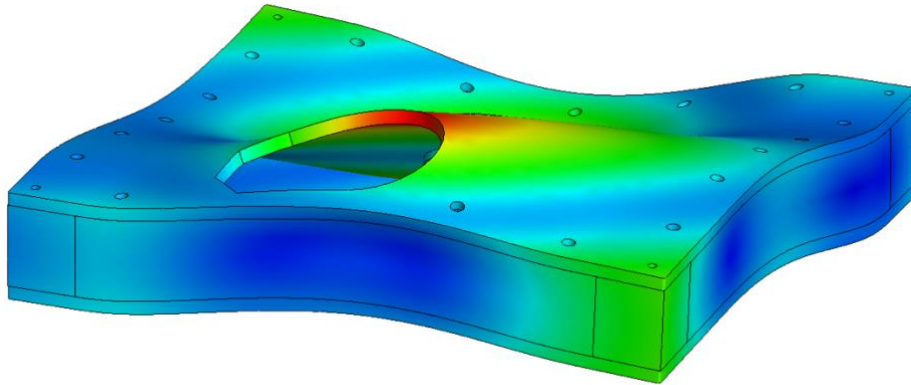


Figure 2.25 – Main Frame, Frequency Analysis, Natural Mode 10

The resonance frequency associated with this modal shape is 197.8 Hz.

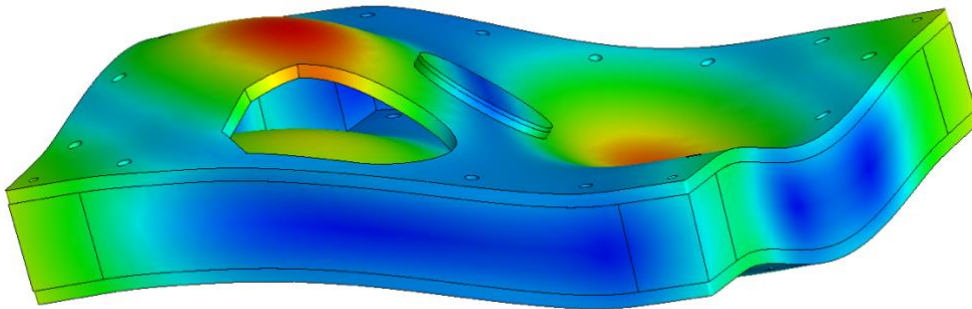


Figure 2.26 – Main Frame, Frequency Analysis, Natural Mode 11

The resonance frequency associated with this modal shape is 197.98 Hz.

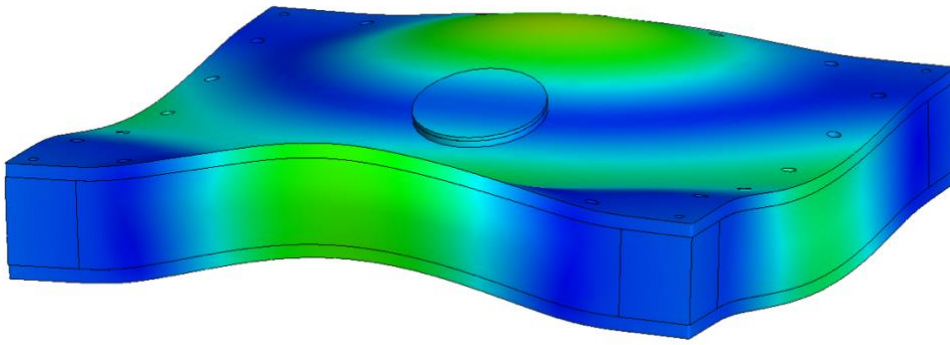


Figure 2.27 – Main Frame, Frequency Analysis, Natural Mode 12

The resonance frequency associated with this modal shape is equal to 205.56 Hz.

As it can be easily noticed, all the resonance frequencies that cause significant deformation are remarkably bigger than the working frequency, so the results of this analysis can be considered satisfactory.

Chapter 3

Test Bench – The Quasi-Static Analysis

From this point on, the work is mainly focalized on the upper part of the bench, the measuring system. The behavior of the system has to be evaluated in terms of lift and drag force and stability. As previously introduced, a specialized system setup is needed in order to quantify the lift and drag forces in quasi-static conditions, i.e. the constant longitudinal velocity and airgap between the pad and the track. In this chapter the layout to perform such analysis will be introduced and described and the configuration and results of the performed analyses will be discussed.

Quasi-Static Test Layout

The main goal of this experiment is to evaluate the lift and drag force to which the magnetic pad is subject due to its interaction with the copper track.

The measurement system chosen to be implemented on the bench in order to perform such assessment consists of two load cells, mounted in such a way that each one can measure respectively the forces causing the lift and the drag strains to which the system is subject.

A load cell is a force transducer, its job is to convert a force such as tension, compression etc. into an electrical signal that can be measured and standardized. One of the most common typologies of load cells consists in strain gauges, which is the kind chosen to be implemented in the quasi-static test layout. Strain gauges measure deformation through a variation in resistance. A strain gauge is basically a metallic foil mounted on a flexible substrate, which also serves the function of insulating the foil, attached to the object under test. A current flows

through the foil pattern and, when the test object is deformed, so is the pattern on the strain gauge, resulting in a variation of its resistance. Measuring such variation it is possible to evaluate the entity of the deformation and determine the value of the responsible forces.

The pad, incased in a proper structure, is linked to the two load cells through two couples of foil springs, that allow respectively the longitudinal and vertical displacements through which the cells determine the lift and drag forces.

The test layout is shown in the following picture. In this paragraph the main components of the system will be identified and described, and design choices will be motivated, following the order of the call-out balloons.

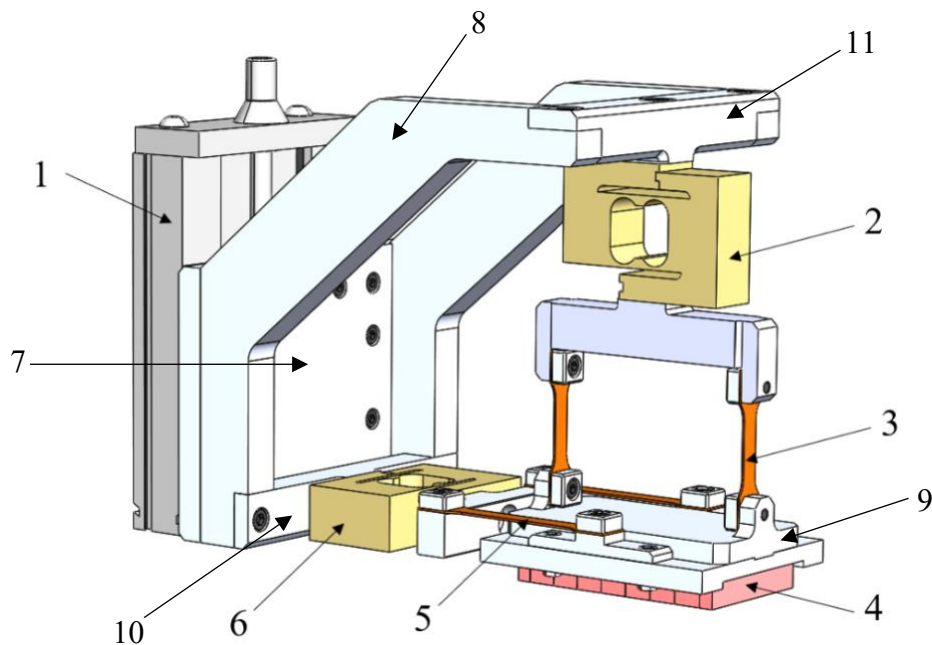


Figure 3.1 - Quasi-Static test layout, 3D model

3. TEST BENCH – THE QUASI-STATIC TEST LAYOUT

1. A linear micrometric stage is implemented in the measurement system to be tuned in order to impose the initial airgap between the PM array and the copper track. The chosen model is the Norelem 21000-120175 [27] with a range of motion equal to 50 mm. The specifics of this component are listed in the following table.

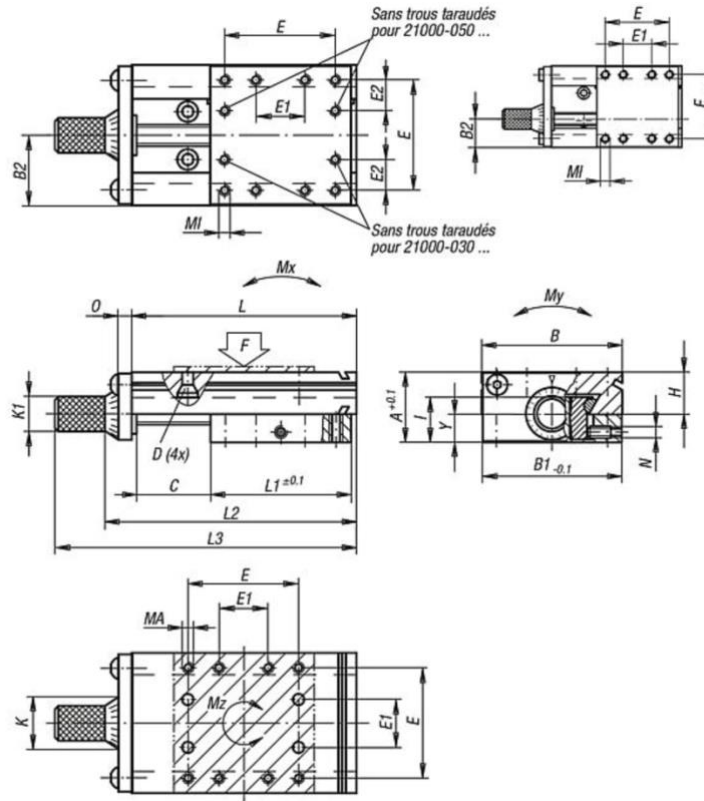


Figure 3.2 – Norelem Linear Stage Drawings

Force F	1500 N
Torque X axis	30 Nm
Torque Y axis	45 Nm
Torque Z axis	18 Nm

Table 3.1 – Norelem Linear Stage Data

3. TEST BENCH – THE QUASI-STATIC TEST LAYOUT

2. The upper load cell serves the function of evaluating the lift force generated from the interaction of the pad with the track. The chosen load cell model is the HBM S2-500 [28], with a dimension of 60 mm x 80 mm x 25.4 mm and a weight of 0.8 kg. The load cells' specifics can be read in the table below.

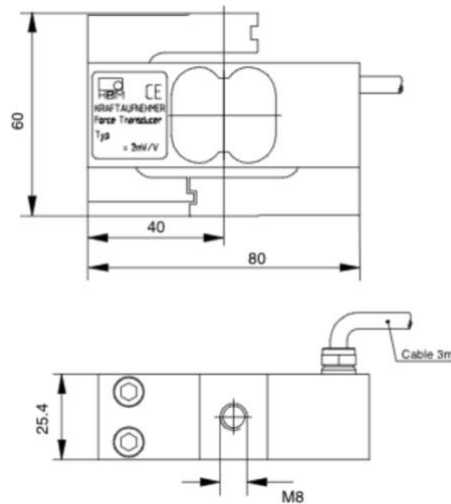


Figure 3.3 – HBM Force Transducer, Drawings

Force transducer type			S2					
Nominal force	F_{nom}	N	20	50	100	200	500	1000
Accuracy class					0.05			
Nominal sensitivity	C_{nom}	mV/V			2			
relative sensitivity deviation tensile/compressive force	d_c	%			± 0.25			
relative tensile/compressive sensitivity difference	d_{zd}	%			$< \pm 0.1$			
relative deviation from zero	$d_{s,0}$	%	< 8	< 6			< 5	
Relative range of inversion ($0.2F_{nom}$ to F_{nom})	u	%			0.1			
Linearity deviation	d_{lin}	%			0.05			
Temperature effect per 10K by reference to sensitivity								
to sensitivity	TK_c	%			0.05			
to zero signal	TK_0	%			0.05			
Effect of transverse forces (transverse force 10% F_{nom}) ^{*)}	d_Q	%			± 0.1			
Effect of eccentricity at 1mm	d_E	%			± 0.1			
Creep over 30 min	d_{crF+E}	%			$< \pm 0.05$			
Input resistance	R_e	Ω			> 345			
Output resistance	R_a	Ω			300 – 500			
Isolation resistance	R_{is}	$G\Omega$			$> 2 \times 10^9$			
Reference excitation voltage	t_{ref}	V			5			
Operating range of the excitation voltage	$B_{U,G,T}$	V			0.5...12			
Nominal temperature range	$B_{t,nom}$	$^{\circ}C$			+10...+70			
Operating temperature range	$B_{t,G}$	$^{\circ}C$			-10...+70			
Storage temperature range	$B_{t,S}$	$^{\circ}C$			-30...+85			
Reference temperature	t_{ref}	$^{\circ}C$			+23			
Maximum operating force	(F_G)	%	120	120		150		
Limit force	(F_L)	%			200			
Breaking force	(F_B)	%			> 300			
Limit torque	(M_d)	Nm	0.6	1.5	3	6	15	15
Static lateral limit force [*]	(F_Q)	%	50		100			50
Nominal displacement	S_{nom}	mm			< 0.4			
Fundamental resonance frequency	f_G	kHz	0.29	0.49	0.76	1.09	1.81	2.45
Relative permissible vibrational stress	F_{rb}	%			± 70			
Weight		kg			approx. 0.4			
Degree of protection to DIN EN 60529					IP65			
Cable length, 6-wire connection		m			3			

^{*)} by reference to a force introduction point on the force-introduction surface

Table 3.2 – HBM Force Transducer Data

3. Two vertical leaf springs, made of Lama Blu Steel, have the function of permitting the longitudinal displacement of the pad caused by the drag force and measured by the lower cell. The springs have a thickness of 1 mm and are shaped as follows:

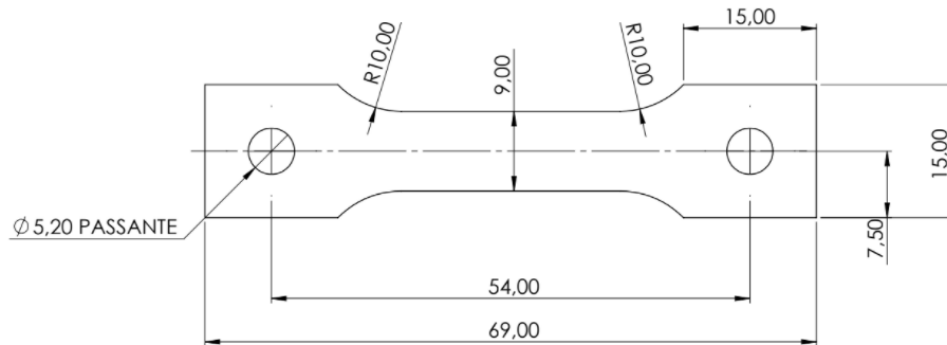


Figure 3.4 – Quasi-Static Test Layout, Vertical Leaf Springs design

4. The Permanent Magnet array, made of neodymium magnets, is placed on the lower surface of the bench, in the position that best guarantees its interaction with the copper track posed on the lower part of the bench. It is made of nine different magnets with different polarizations, arranged in a specific configuration such that they generate a periodic field on the surface facing the copper track. All the magnet have length equal to 63.5 mm and width equal to 12.7 mm, the ones located at the two limits of the pad have width equal to 6.35 mm while all the internal ones have width equal to 12.7 mm. The orientation of each magnet follows the scheme reported in the figure.

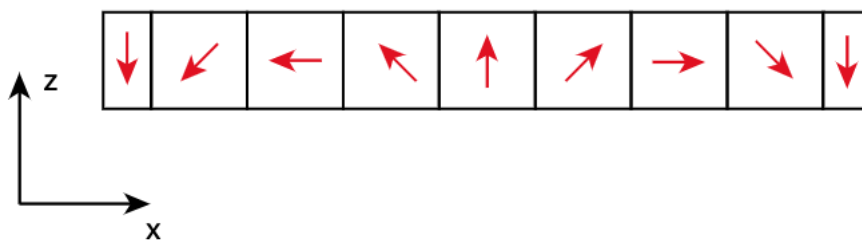


Figure 3.5 – Magnets Arrangement

5. Two horizontally placed leaf springs, posed between the structure supporting the magnetic pad and the one supporting the lower load cell, serve the purpose of permitting the vertical displacement to be measured by the upper cell. The springs are made of Lama Blu Steel with a thickness of 1 mm and are shaped as follows.

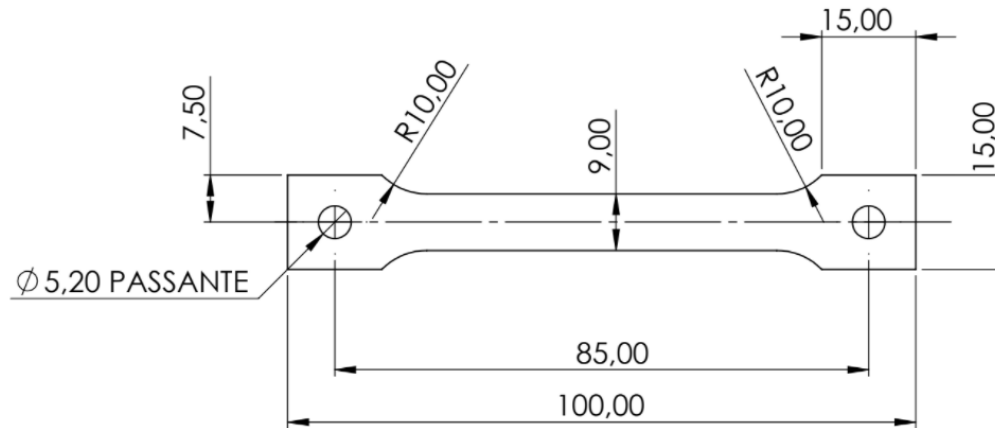


Figure 3.6 – Quasi-Static Test Layout, Horizontal Leaf Springs design

6. The lower load cell has the purpose of evaluating the drag force through the longitudinal displacement of the pad. The specifics are the same as the vertical on (2.) because the chosen model is the same, *i.e.* the HBM S2-500 [28], with a dimension of 60 mm x 80 mm x 25.4 mm and a weight of 0.8 kg. They have a nominal force of 500 N.

7. A specific component is designed to implement the linear stage into the system. To serve this purpose, the stator replies the shape of the moving part of the linear stage and it is provided with corresponding holes to the ones present on it, so that they can be hooked. Additional holes are placed on the other side of the stator to link it with the proper components of the bench, too. The stator has a thickness of 15 mm and it is designed as follows. It is built of Ergal.

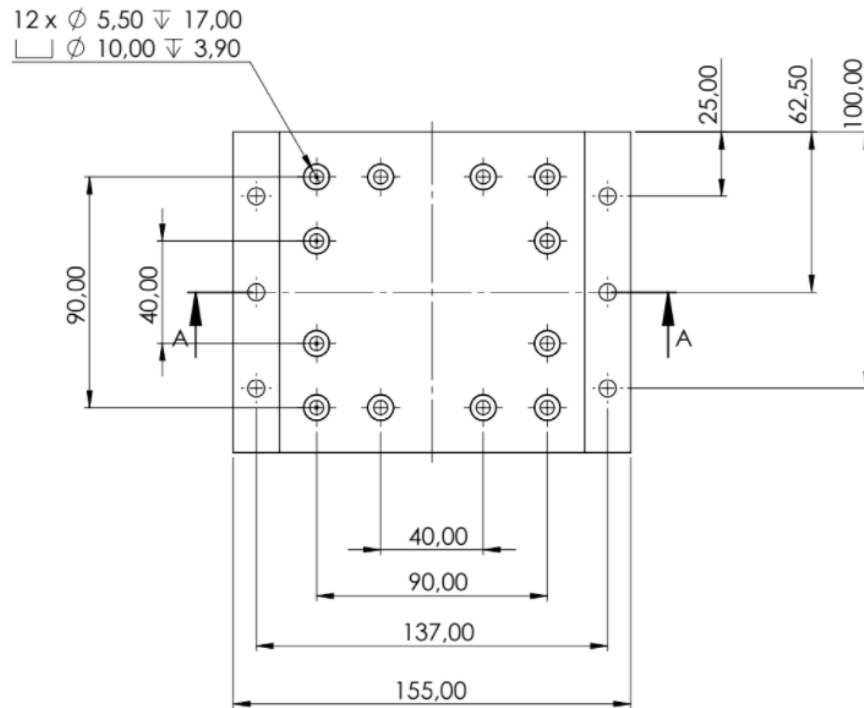


Figure 3.7 – Quasi-Static Test Layout, Stator 7. Design

8. Two stators are designed to sustain the upper load cell and the vertical spring arrangement and link this subsystem to the stage. They have an overall length of 206 mm and width of 203 mm, and an inclination of 50.57° . The material chosen to produce these components is Ergal.

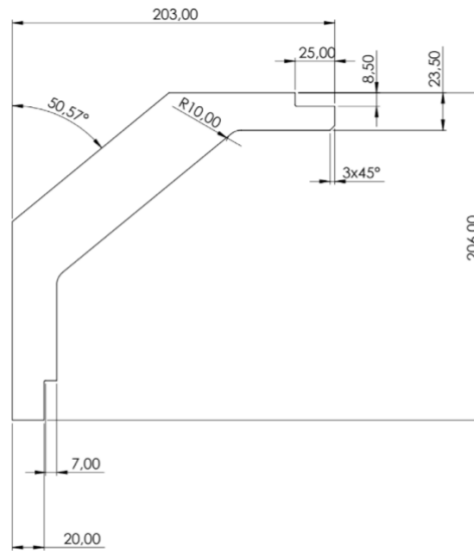


Figure 3.8 – Quasi-Static Test Layout, Stator 8. Design

9. The structure designed to house the PM pad is made of two coupled components, the upper one has the purpose to connect the structure to both the horizontal and vertical spring systems, while the lower one has the sole purpose to house the pad and connect it to the bench. The two components are made of Ergal and they both have a length of 116 mm to contain the entire pad, which has a length of 101.6 mm.

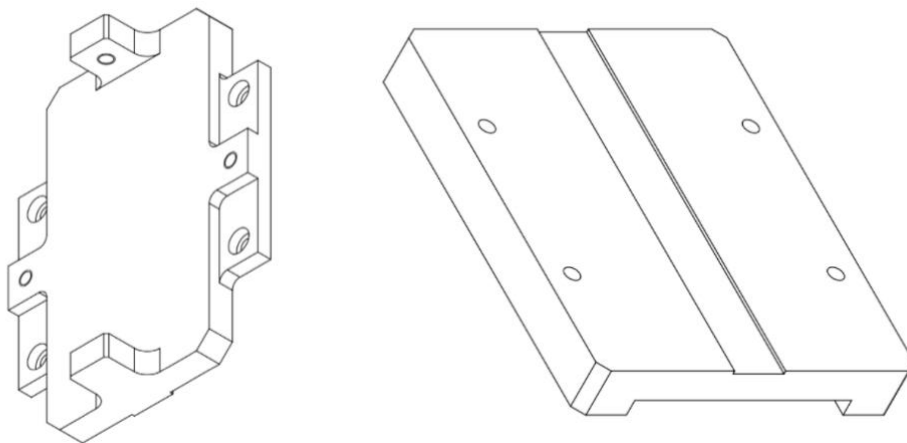


Figure 3.9 - PM Pad Housing, upper and lower components

10. A stator is needed to bind the lower load cell to the linear stage. This stator is built in Ergal and has a length of 155 mm, to cover all the width of the linear stage. The design phase of this component includes a testing phase that will be covered afterwards.
11. Another stator is designed to bind the upper cell to the stators linking it to the linear stage. This stator also follows the dimensions of the stage with a length of 155 mm and it is made of Ergal. This design, too, has been submitted to a virtual testing procedure before getting into production.

Stators, Static Deflection

As previously discussed, numerous stators are needed to support the load cells and bind them to the static part of the system. These components are subject to consistent loads due to the displacements caused by the interaction of the pad with the rotating runway, hence the need to subject them to a Linear Static Analysis, to ensure that their static deformation doesn't affect the behavior of the system.

The first component to undergo such test is the stator connected to the lower load cell. The parameters to be set for performing the simulation, as mentioned in the previous chapter, are fixed as follows:

- The material with which the component is built is Ergal, so it is chosen to associate it, among the SolidWorks proposed choices, the aluminum alloy 2024-T3, with elastic modulus equal to 7.24×10^{10} N/m² and mass density coefficient equal to 2780 kg/m³;
- A fixed geometry constraint is placed on the two portions of the surface that interact with the 8. stators linking them to the linear guide, hence imposing the constraint in the real environment;

3. TEST BENCH – THE QUASI-STATIC TEST LAYOUT

- A load equal to 250 N is placed on the portion of the surface interacting with the load cell. In the real experiment this component works with a 200 N ca. load, so a safety factor of 1.25 is implemented for conservative reasons. The obtained configuration looks as follows.

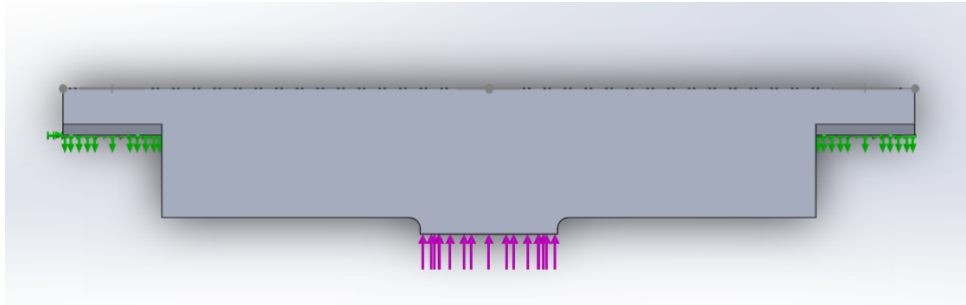


Figure 3.10 – Quasi-Static Test Layout, Stator 11., Linear Static Analysis, conditions

- The mesh is created according to the geometry of the component.

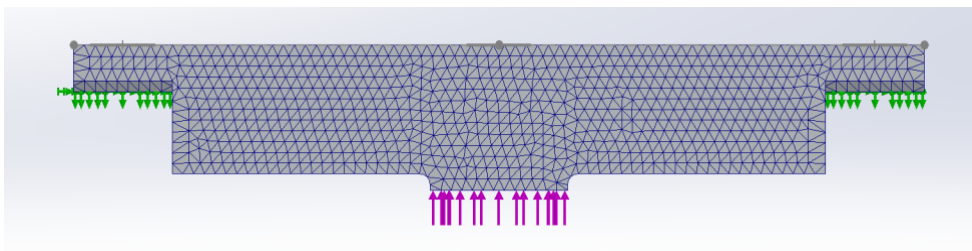


Figure 3.11 – Quasi-Static Test Layout, Stator 11., Linear Static Analysis, Mesh

The simulation can now be performed and the results are shown in the following picture.

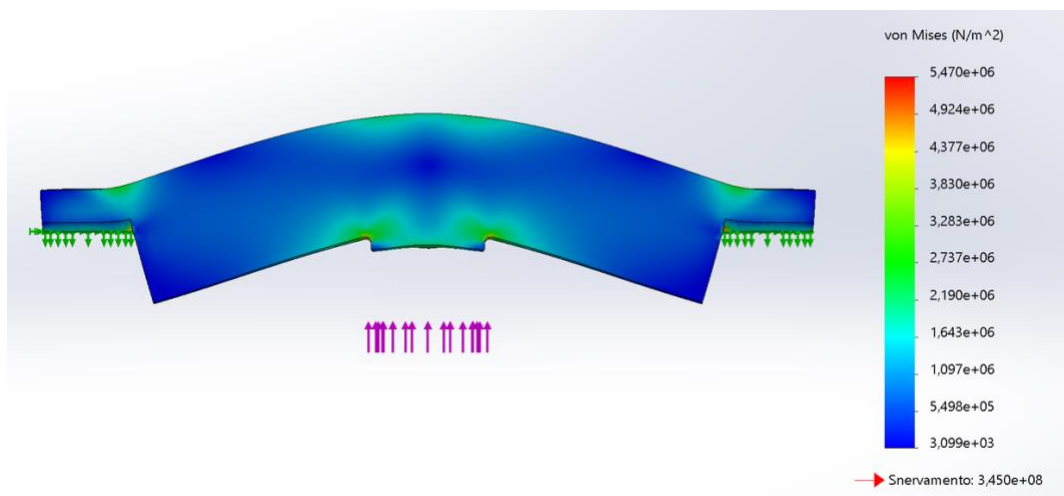


Figure 3.12 – Quasi-Static Test Layout, Stator 11., Linear Static Analysis, Results

The maximum deformation resulting from the simulation is equal to $3.899\text{e-}6$ m, which is considered a satisfactory response.

As it can be noticed in the picture, the yielding limit tension of the chosen material is significantly superior to the stress values detected.

The stator supporting the lower load cell is now object of analysis. The parameters are set as follows:

- As in the previous case the chosen material is the aluminum alloy 2024-T3, with elastic modulus equal to $7.24 \text{ e+}10 \text{ N/m}^2$ and mass density coefficient equal to 2780 kg/m^3 ;
- A fixed geometry constraint is imposed on the two surfaces interacting with the two 8. stators linking the component to the linear guide.
- A load equal to 150 N is applied to the surface interacting with the load cell. In the real experiment this component works with a 100 N ca. load, so a safety factor of 1.5 is implemented for conservativity reasons.

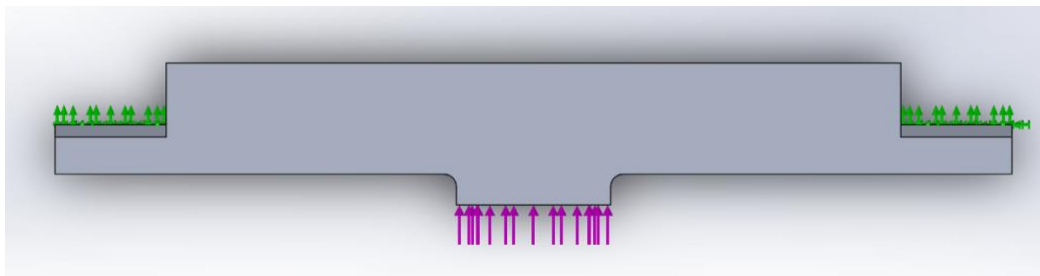


Figure 3.13 – Quasi-Static Test Layout, Stator 10., Linear Static Analysis, conditions

- The mesh is generated according to the geometry of the component.

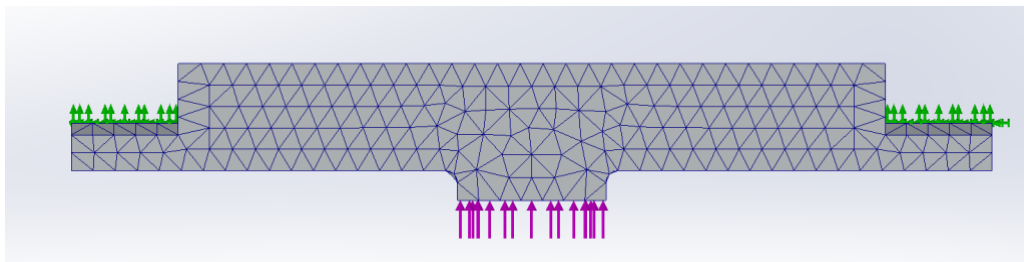


Figure 3.14 – Quasi-Static Test Layout, Stator 10., Linear Static Analysis, Mesh

Finally, the simulation can be performed and the deformed result is represented in the following picture.

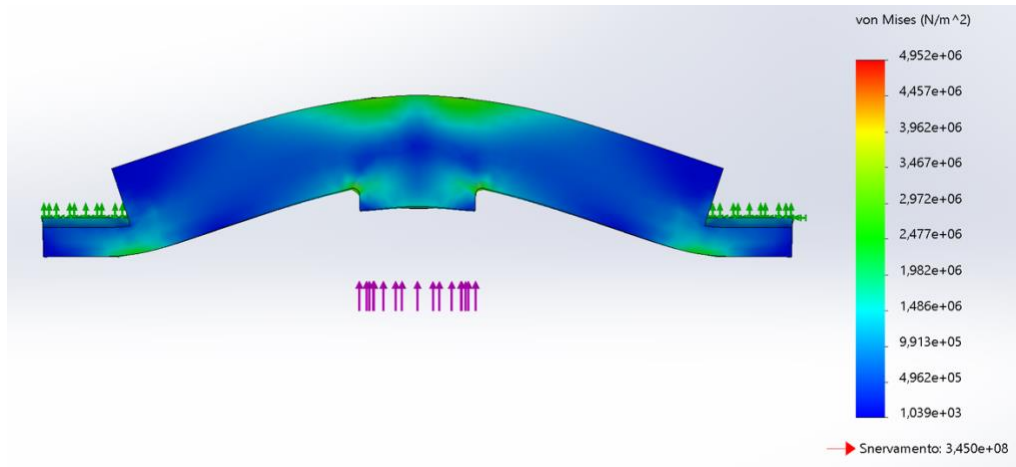


Figure 3.15 – Quasi-Static Test Layout, Stator 10., Linear Static Analysis, Results

The maximum value of the deformation resulting from the simulation is $3.033\text{e-}6$ m, which is considered satisfactory and safe for the right development of the experiment.

As it can be appreciated from the picture, the design is safe also in terms of stress, since the yielding limit tension of the material, reported in the bottom-right corner of the picture, is far higher than the stress level reached in the simulation.

Finally, the twin 8. stators are subject to Linear Static Analysis, to detect how the load due to the lift force affects their shape and behavior.

The parameters for correctly performing the simulation are set as follows:

- As in the previous cases the chosen material is the aluminum alloy 2024-T3, with elastic modulus equal to $7.24 \text{ e}+10 \text{ N/m}^2$ and mass density coefficient equal to 2780 kg/m^3 ;
- A fixed geometry constraint is placed all over the back surface of the piece, right when the contact with the stator 7. occurs.

- These two stators work with a 100 N ca. load each, because they react to the behavior of the stator 11. previously studied. For safety reasons a 1.5 safety factor is applied, so on the contact surface between stator 8. and stator 11. a load of 150 N is imposed.

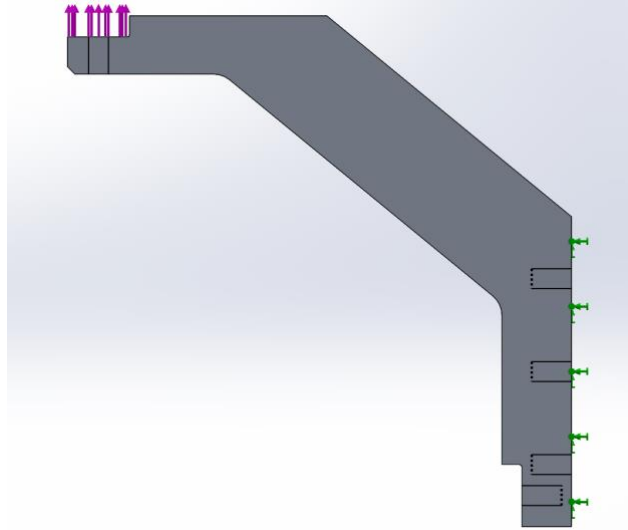


Figure 3.16 – Quasi-Static Test Layout, Stator 8., Linear Static Analysis, Conditions

- The mesh is generated according to the geometry of the component.

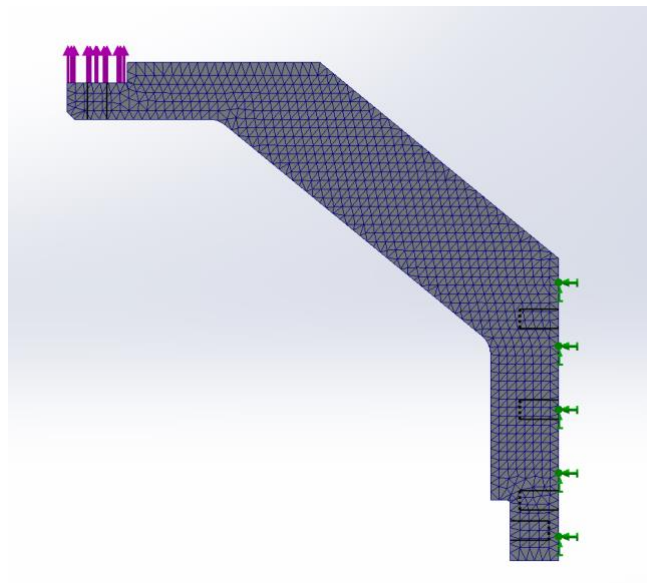


Figure 3.17 – Quasi-Static Test Layout, Stator 8., Linear Static Analysis, Mesh

At this point the simulation can be run and the results are the following.

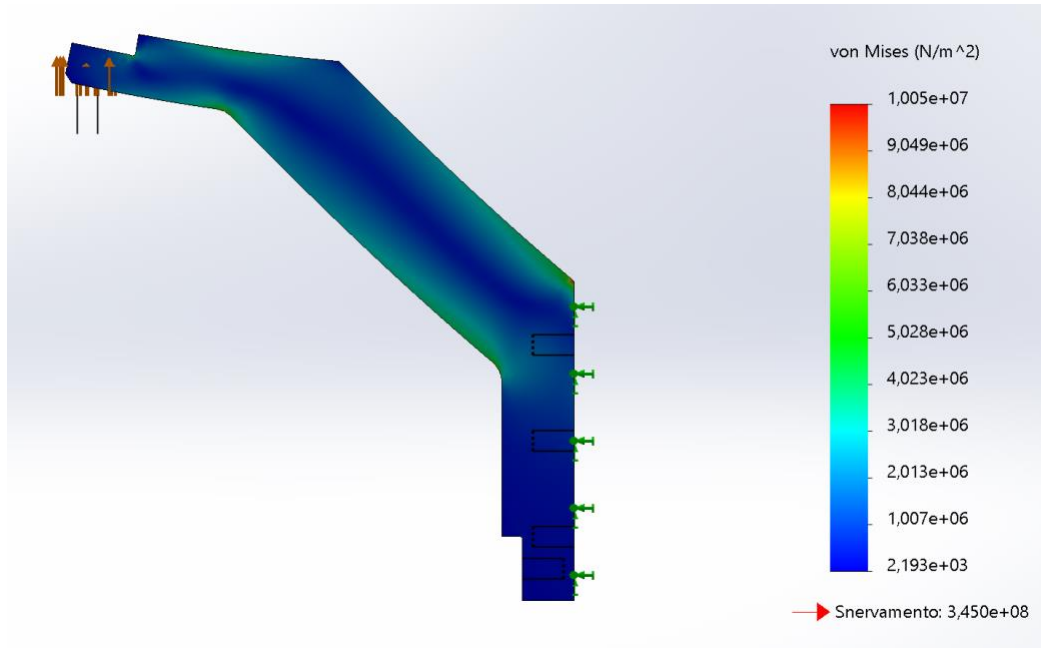


Figure 3.18 – Quasi-Static Test Layout, Stator 8., Linear Static Analysis, Results

The maximum deformation value resulting from the simulation is 5.917×10^{-5} m, considered a satisfying value since it doesn't affect significantly the geometry and behavior of the system, moreover, the results are considered satisfying also in terms of stress, since the yielding limit tension of the chosen material, shown in the bottom-right corner of the picture, is significantly higher than all the stress values to which the structure is subject, according to the analysis.

Quasi-Static Test Layout, Modal Analysis

As previously explained, this layout is designed to measure lift and drag forces by means of vertical and horizontal displacements, hence, being the system subject to dynamic behavior, the need to perform a frequency analysis in order to detect and evaluate its natural vibration modes.

The parameters for performing this kind of simulation, discussed in the previous chapter, are set as follows:

- The material chosen for the large majority of the components is Ergal, hence the decision to assign to these, among the SolidWorks proposed choices, the aluminum alloy 2024-T3, with elastic modulus equal to 7.24×10^{10} N/m² and mass density coefficient equal to 2780 kg/m³;

- The material assigned to the load cells (Steel), the leaf springs (Lama Blu Steel) and the pad (Neodimium) is Carbon Steel, with an elastic modulus of $2.1 \text{ e}+11 \text{ N/m}^2$ and a mass density coefficient equal to 7800 kg/m^3 .
- A fixed geometry constraint is placed all over the back surface of the stator linking the system to the linear guide, simulating its behavior, as can be seen in the following picture.

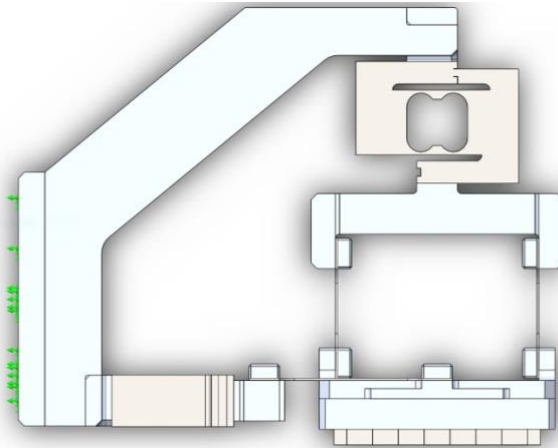


Figure 3.19 – Quasi-Static Test Layout, Frequency Analysis, Constraints

- The mesh is generated tuning its density to the dimension and shape of the single components.

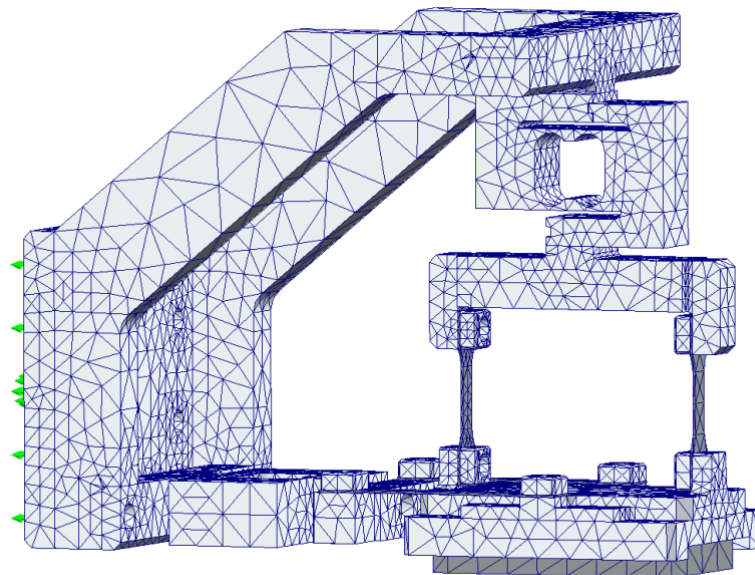


Figure 3.20 – Quasi-Static Test Layout, Frequency Analysis, Mesh

The frequency analysis is performed, resulting in the following data and configurations. The first 10 natural modes and shapes are described. A remark is needed of the fact that, in order to

3. TEST BENCH – THE QUASI-STATIC TEST LAYOUT

work in safe conditions and to prevent significant damage to the equipment, all the resonance frequencies need to be higher than the working frequency which is equal to 1.5 Hz.

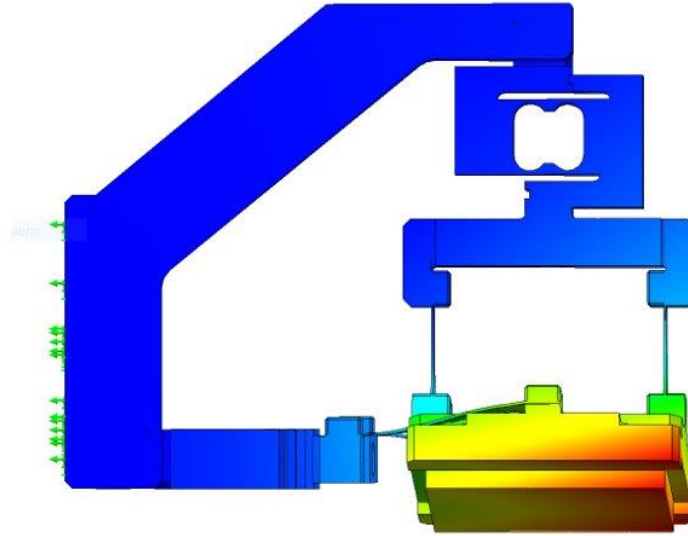


Figure 3.21 – Quasi-Static Test Layout, Frequency Analysis, Natural Mode 1

The resonance frequency associated with this modal shape is 79.377 Hz.

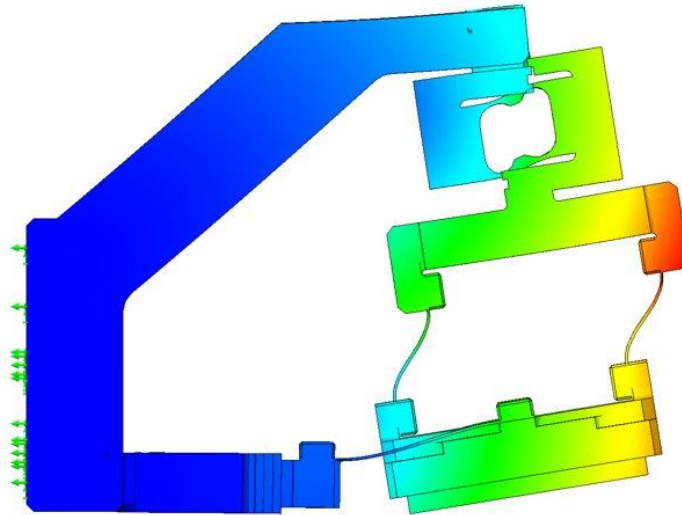


Figure 3.22 – Quasi-Static Test Layout, Frequency Analysis, Natural Mode 2

The resonance frequency associated with this modal shape is 168.95 Hz.

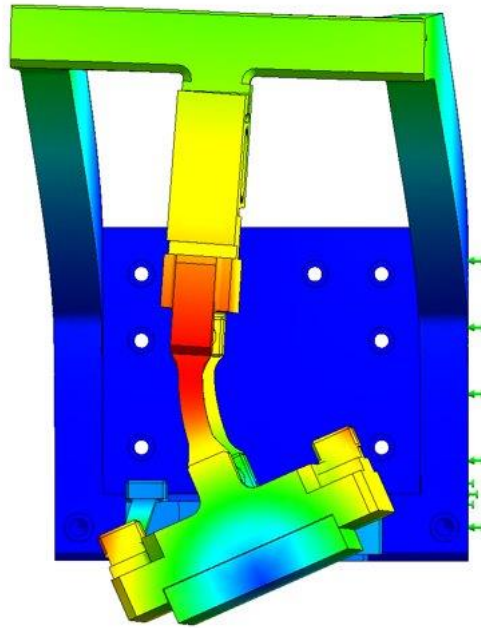


Figure 3.23 – Quasi-Static Test Layout, Frequency Analysis, Natural Mode 3

The resonance frequency associated with this modal shape is 197.31 Hz.

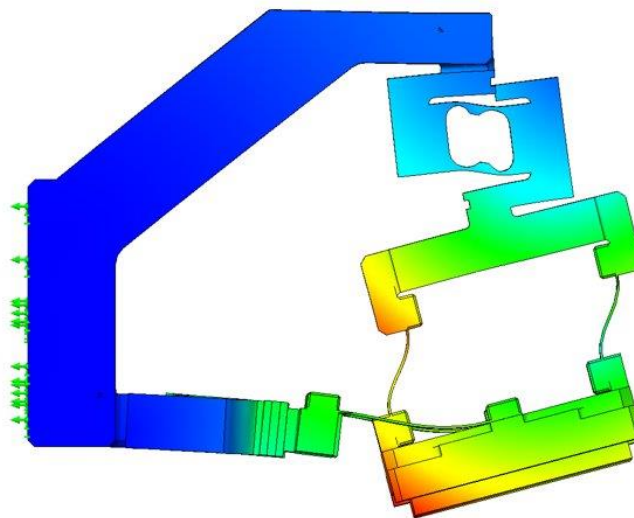


Figure 3.24 – Quasi-Static Test Layout, Frequency Analysis, Natural Mode 4

The resonance frequency associated with this modal shape is 218.49 Hz.

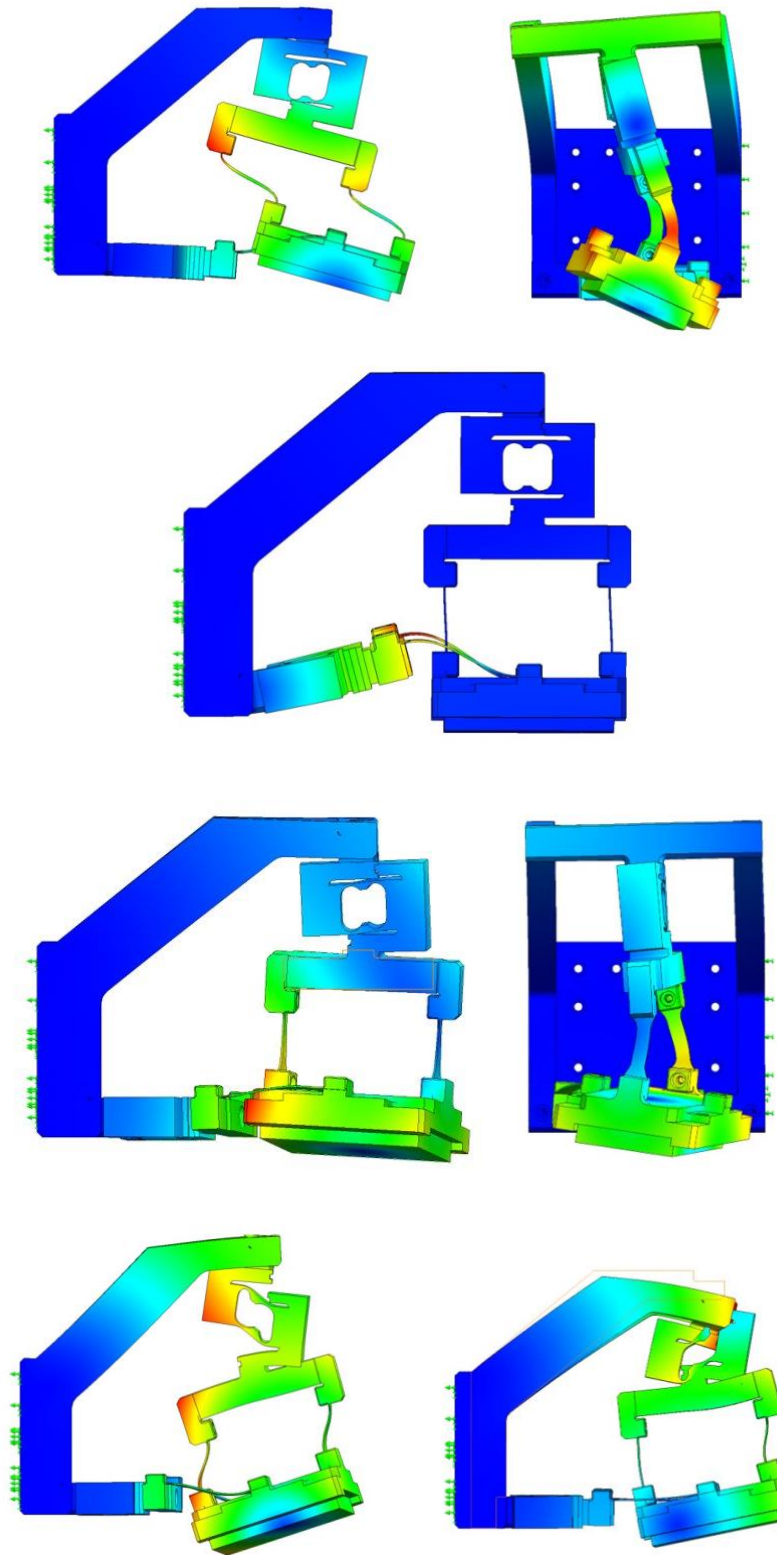


Figure 3.25 – Quasi-Static Test Layout, Frequency Analysis, Further Natural Modes

The resonance frequency values associated with these last modal shapes belong to higher orders of magnitude, hence are considered non-significant for the purposes of this experiment.

Considering the results of this analysis and the high values of all the resonance frequencies with respect to the working frequency of 1.5 Hz, it is safe to say that the work is being carried out in optimal conditions and the design is effective and ready to get into production.

Quasi-Static Test Layout, Assembling

Once the system is designed and verified, it is time to realize it. The commercial components are purchased and the remaining need to be manufactured. The latter are drafted and dimensioned and the drawings are shared with the workshop in charge of producing the pieces.

After the manufacturing of the components the system is assembled. The assembly of all the manufactured components is shown in the following pictures.

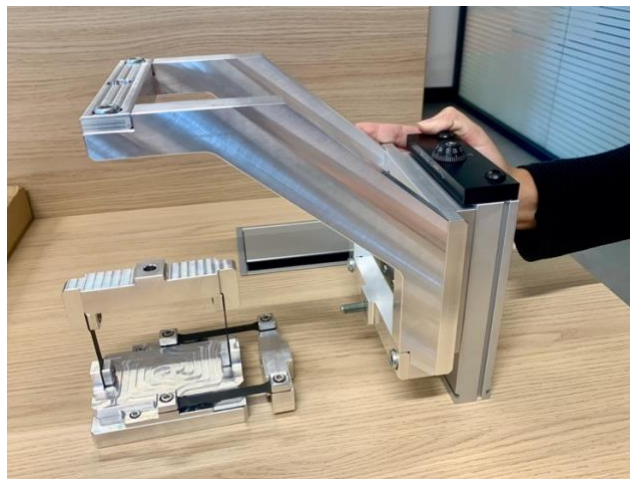


Figure 3.26 – Quasi-Static Test Layout, Assembling



Figure 3.27 – Quasi-Static Test Layout, Assembling

After building the latter subsystem the magnets need to be placed in their specific housing. As previously explained, the magnets present different polarizations, so they tend to attract each other in a way that makes it difficult to place them in the right configurations. Their magnetic charge is extremely powerful and the extension of the contact surfaces is considerable, therefore the chance that they interact in a non-controlled way represents a significant danger for the right development of the experiment and to those who work on the project.

In order to avoid the occurrence of these circumstances, a jig is designed to facilitate the insertion of the magnets in the proper housing and prevent their interaction in other ways than the ones planned. The jig is composed of two elements shaped as follows.

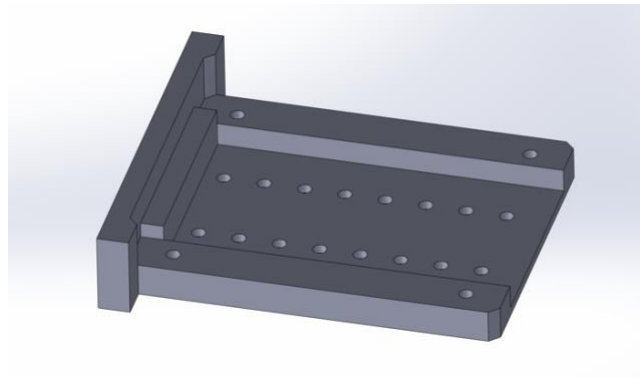


Figure 3.28 – Magnetic Pad Jig, Element 1

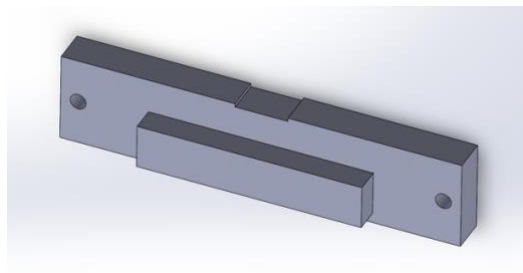


Figure 3.29 – Magnetic Pad Jig, Element 2

The first element appears like a drawer that will be mounted on the bottom of the stator supporting the pad. The depth of the internal part is equal to the width of the magnets, so that, once inserted, they are not able to rotate and interact differently than planned. Once this part is mounted, the magnets are inserted one at a time and the jig is closed with the element shown in the second picture. Afterwards, glue can be injected through the holes on the bottom of the jig

in order to fix the magnets in the planned position. This jig is likely to be 3D printed in PLA. The position in which the jig will be mounted on the system is shown in the following picture.

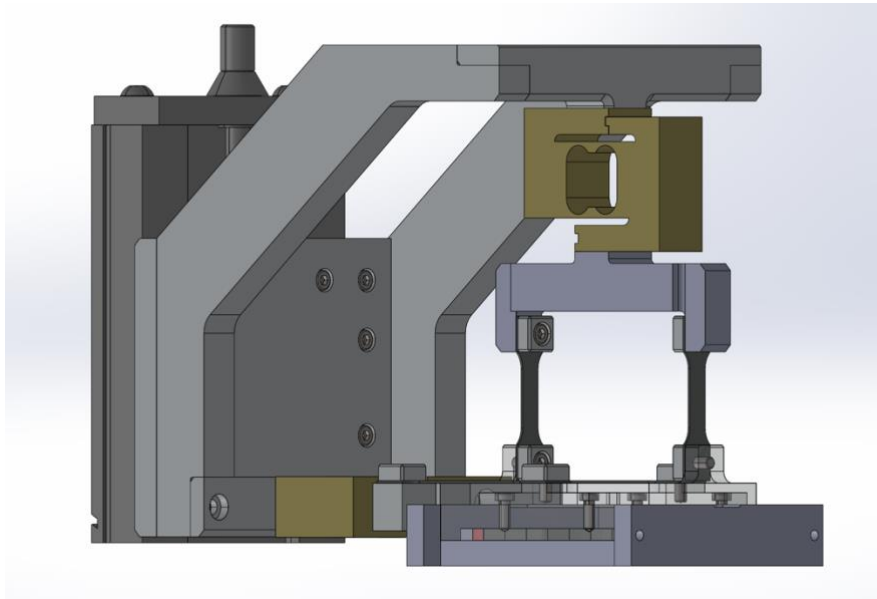


Figure 3.30 – Quasi-Static Test Layout, Jig Implementation

Chapter 4

Test Bench – The Dynamic Analysis

A different test layout is needed to perform the dynamic analysis of the system and study its stability.

In this chapter the layout of such system will be described through the different phases that lead to the final design. The differences between this setup and the one previously described will be highlighted and motivated. In particular, an identification of the main components will be provided, along with the description and results of the frequency analysis carried out on the system and the drawings of the ensemble and all the singular pieces.

Dynamic Test Layout, Design Procedure

The setup designed to evaluate the dynamic behavior of the system can be simplified as a quarter car model. In fact it features a sprung mass (3) an unsprung mass (7), a spring with stiffness k_s (6), a damper with damping factor c_s (4) between the sprung and the unsprung mass, a secondary spring with stiffness k_{us} (5) between the unsprung mass and the stator (1) and finally the PM pad (2) attached to the unsprung mass.

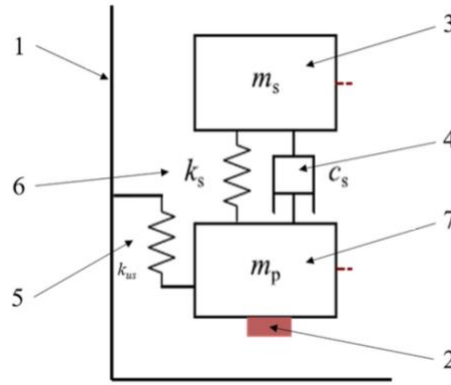


Figure 4.1 - Dynamic Test Layout, 2D model

As in the previously discussed Quasi-Static test layout, the pad interacts with the copper track placed in the main frame of the system, causing the levitation of the whole upper subsystem, therefore a mass-spring-damper arrangement is needed to stabilize the levitation.

Different modellings of the system, increasingly precise and complex as the research work proceeded, lead to the final design to be realized and tested. In this section all the design steps will be discussed and analyzed, motivating the modifications between one another and showing how the design was adjusted as more information was provided by the research team. All of the CAD drawings were produced in SolidWorks environment.

The first 3D model of the system is represented in the following picture.

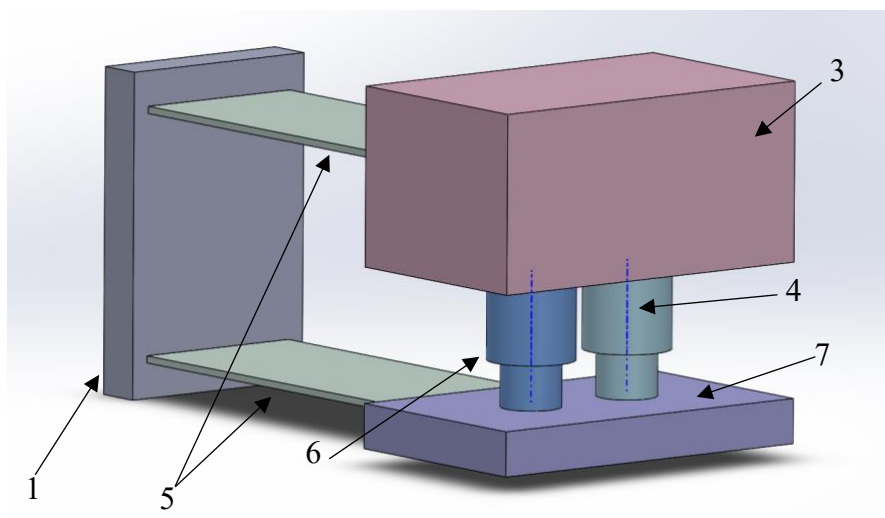


Figure 4.2 - Dynamic Test Layout, 3D model

This model, designed in an early stage of the process, features two foil springs linking both the sprung and the unsprung mass to the stator. The damping system is represented qualitatively through two couples of concentric cylinders, embodying the spring (6) and the damper (4), while the stator (1), the sprung (3) and the unsprung (7) masses are straightforwardly represented through rectangular boxes. The aim of this qualitative model is to give a first idea of the system's structure and geometry.

The following step in the design procedure is shown in *Figure 4.3*.

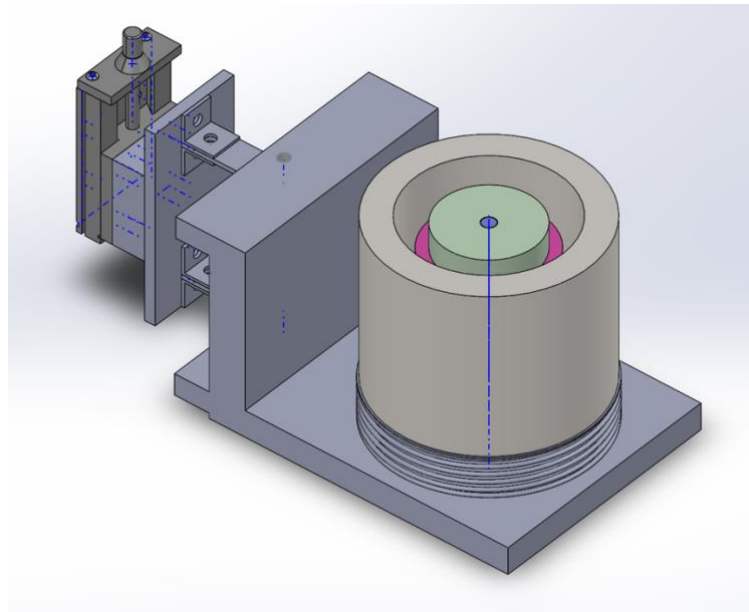


Figure 4.3 - Dynamic Test Layout, 3D model

At this point in the process more details of the design have been defined. The same linear micrometric stage used for the quasi-static test layout will be tuned before starting the experiment, to define the initial airgap between the pad and the track. The spring assumes a helicoidal shape while the secondary suspension function is pursued by a voice coil.

A secondary suspension is needed to compensate the static deformation caused on the elastic connections by the weight of the sprung mass and to guarantee the best stability margins possible to the system, obtained with a quantified optimal damping coefficient c_{opt} equal to 250 Ns/m. The choice falls on the voice coil technology because, unlike oil or elastomer based viscous dampers, it doesn't need to be subject to accurate thermal feasibility analysis before being employed. Additionally, this kind of device guarantees higher precision and flexibility in control [22].

The drawing stays mainly qualitative, as the voice coil is still modeled with two concentric cylinders, which dimensions correspond to the ones of the chosen voice coil, later to be described, and a steel coat is added to reach the desired mass proportional to the pad and the rest of the system.

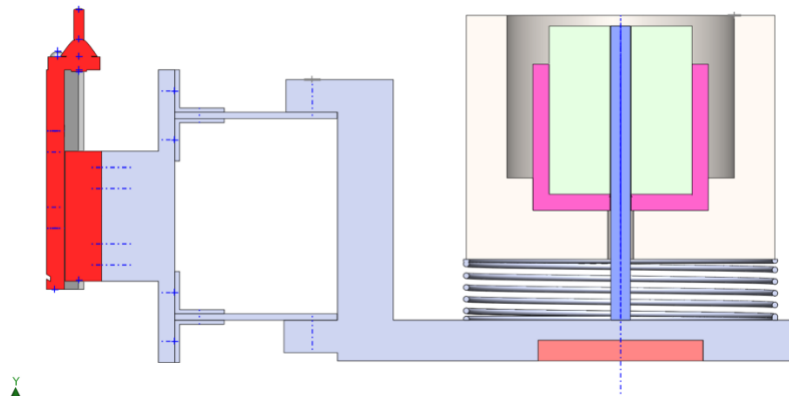


Figure 4.4 - Dynamic Test Layout, 3D model

Design conditions require a total mass, comprehensive of sprung and unsprung, of 22 kg [7], hence, in order to respect the quarter car model proportions ($m_s = 10m_p$), the unsprung mass needs to weigh 2 kg while the sprung mass is equal to 20 kg.

The pad is still represented like a parallelepiped and inserted in a specific housing at the bottom of the system.

The parallelepiped previously representing the linear stage is replaced by the official CAD model of the stage and an appropriate stator is designed to link the unsprung mass only to the stage by means of brackets. An alternative version of this layout is depicted in *Figure 4.5*.

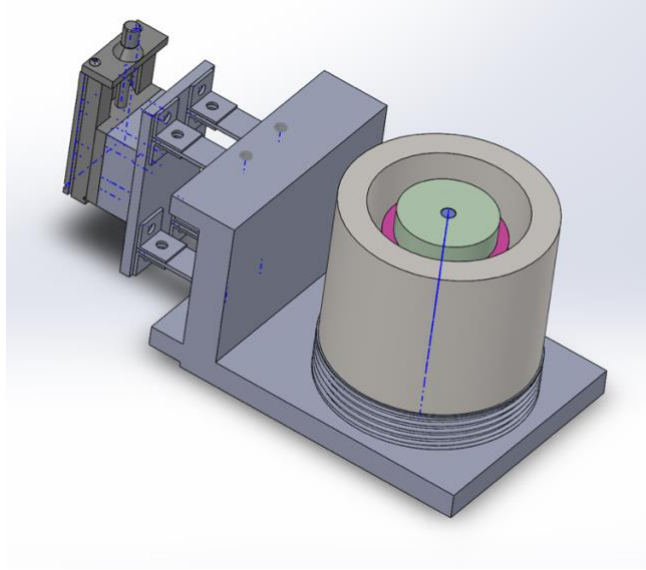


Figure 4.5 - Dynamic Test Layout, 3D model

The previous configuration, with a single column of leaf springs, gave rise to a torsional natural mode of vibration and, consequently, to unpredictable airgap variations. For the purpose of solving this issue the link between the unsprung mass and the stage is doubled, with two parallel columns of leaf springs, to be designed accordingly in order not to alter the global stiffness coefficient k_{us} .

The next design stage is far more specific and detailed and it is presented in *Figure 4.6*.

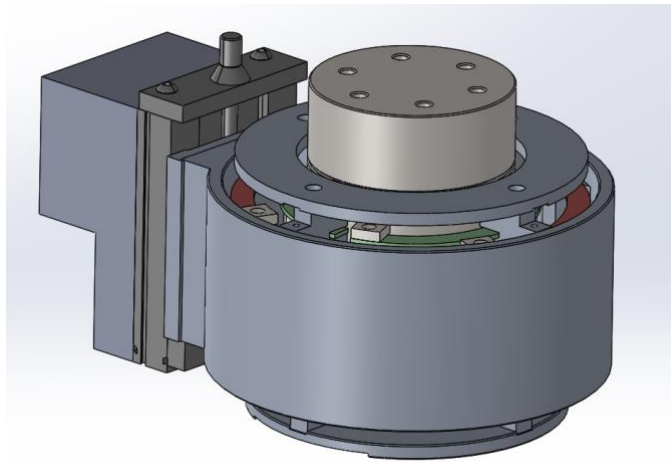


Figure 4.6 - Dynamic Test Layout, 3D model

The main improvement reached in this design with respect to the previous ones is represented by the springs system. In particular, a helicoidal spring, like the one used in the previous model,

yields relative rotation between the two bodies it links, inevitable when a vertical displacement is performed. As a consequence, an arrangement was designed which consists of two concentric layers of curved leaf springs, each one with two rows of four springs each, with the purpose of preventing relative rotation and longitudinal displacement between the two linked parties. The external layer of springs connects the unsprung mass with the stator (rigidly coupled with the linear micrometer stage), while the internal one links the sprung mass to the unsprung mass. A section view is needed to better visualize the layout. The springs (in red and green) are represented qualitatively.

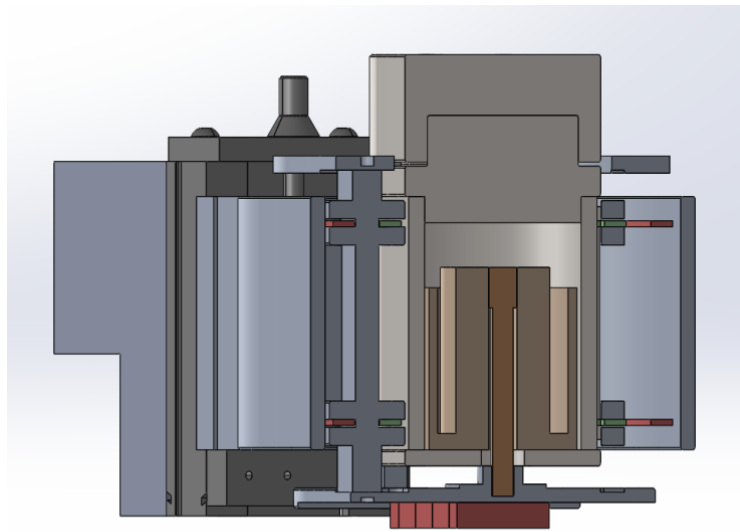


Figure 4.7 - Dynamic Test Layout, 3D model

The stator to which the PM pad is attached is made thinner so that the weight doesn't affect significantly the total value of the unsprung mass, of which the array is the main factor. With this configuration, considering the above-described proportion, the overall weight of the system becomes much lower.

The voice coil is still represented qualitatively.

In this representation a block attached to the linear stage appears. It represents the rigid connection between the fixed part of the stage and the main frame of the bench to serve as reference for the micrometric displacements the stage will impose on the system.

For the next phase the design was enhanced in order to be more practical and easier to manufacture. The design is very close to the final configuration except for the representation

of the voice coil, still qualitative. The results are presented in the following pictures, along with the identification of every one of the above discussed components into this final environment.

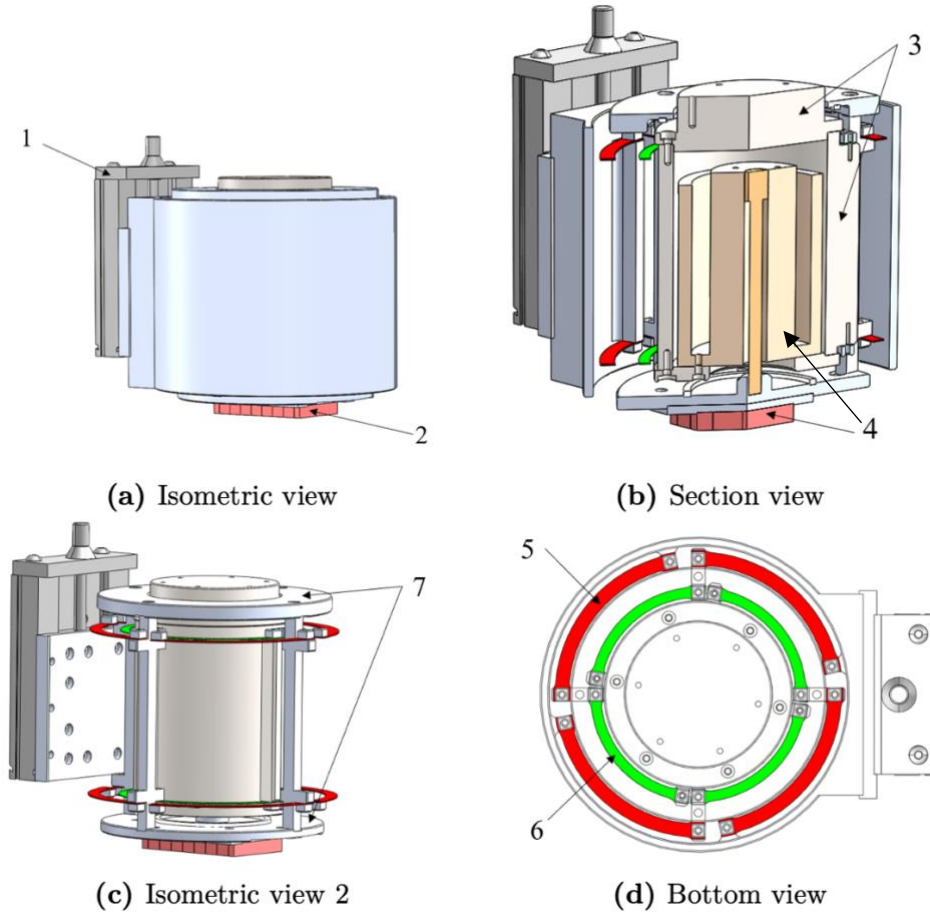


Figure 4.8 - Dynamic Test Layout, 3D model

1) Linear micrometric stage; 2) PM array; 3) Sprung mass; 4) Voice Coil; 5) Unsprung mass-Stator spring layer; 6) Sprung-Unsprung mass spring layer; 7) Unsprung mass.

The subsequent evolution stage bends up being the final design and CAD representation of the layout, featuring a specifically detailed structure and both the official CADs of the two commercial pieces, the linear micrometer stage and the voice coil. The CAD model is shown in the following picture.

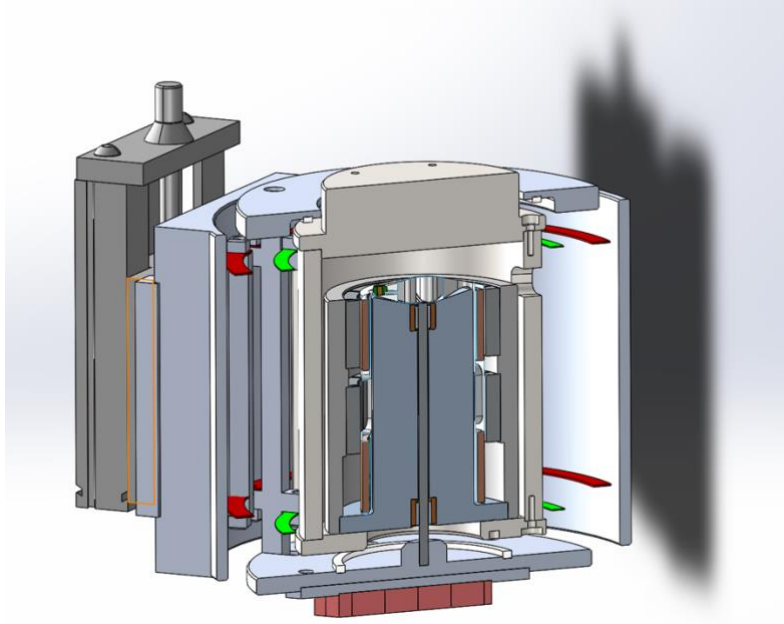


Figure 4.9 - Dynamic Test Layout, Final Configuration, 3D model

A section view was preferred since the main difference dwells in the substitution of the qualitative representation of the voice coil with the official CAD of the chosen model.

Dynamic Test Layout

The system is designed in such a way that most of the commercial components can be used for both the quasi-static and dynamic analyses. This is the case for the linear micrometric stage and the magnetic pad, which are the same used for the setup described in the previous chapter.

As anticipated, a further commercial element needs to be purchased and implemented in this test layout, the Voice Coil. This component has two main tasks, it has to perform a continuous balancing of the weight of the sprung mass (≈ 200 N) and synthesize a variable resistance to produce the needed damping. The former task represents a constraint according to which the choice of the right Voice Coil has been made, selecting a model able to produce a proper value of continuous force capable of equilibrating the static load of the sprung mass, as show in the following chart.

4. TEST BENCH – THE DYNAMIC TEST LAYOUT

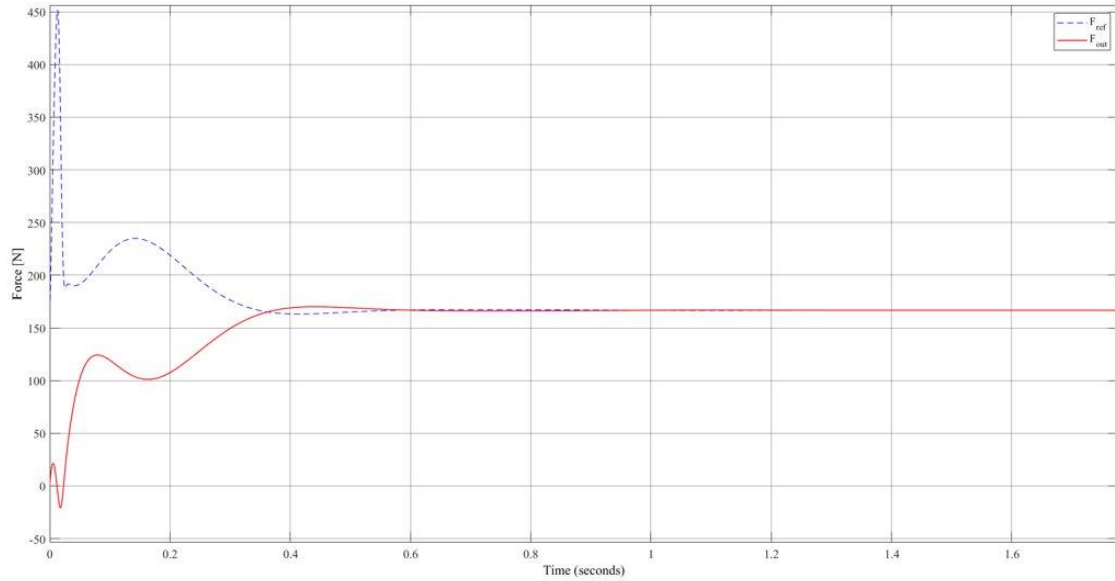
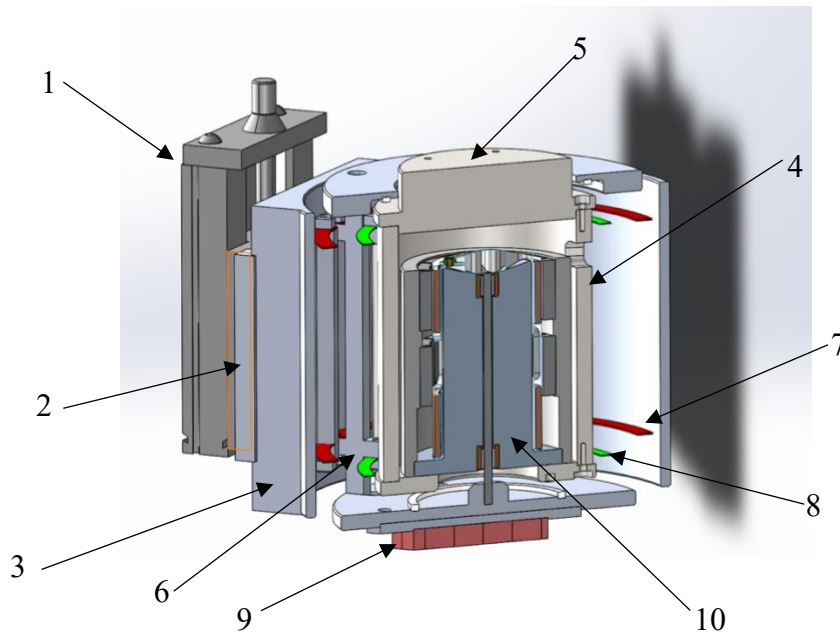


Table 4.1 – Comparison Between the Desired Force and the Voice Coil Output

The large discrepancy at power up is due to the still low longitudinal velocity, which yields too low levitation forces. The steady-state value is achieved at about 0.4 s.

In this section all the main components of the final layout will be identified and described following the order of the call-out balloons presented in the following picture.



1. As anticipated, the Norelem 21000-120175 linear micrometer stage is used for both the test layouts, therefore refer to p.24-25 (1.) for an accurate description.
2. The system is designed so that also the stator bonded to the stage can be used for both the tests, therefore refer to p.28 (7.) for an accurate description.

- This stator has the purpose of connecting the unsprung mass to the linear stage. Thanks to its shape it surrounds the whole system and it features the brackets to which the springs connecting the unsprung mass to the stator itself are fixed. It is built of Ergal and it is designed as follows.

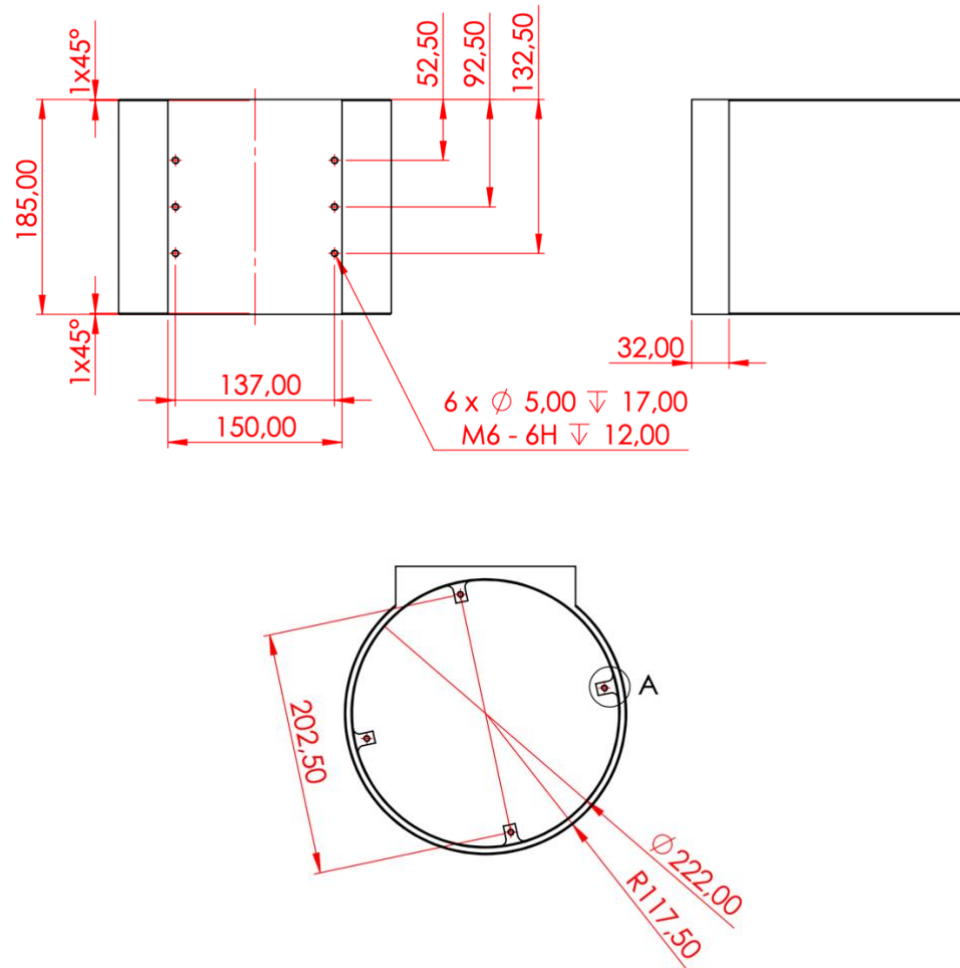


Figure 4.10 - Dynamic Test Layout, Stator 3. Design

4. The purpose of this component is twofold, firstly it contributes to the total weight of the sprung mass, guaranteeing that it reaches 20 kg, in addition it features four reinforcements used to house the springs connecting the sprung mass to the unsprung mass. It is made of Ergal and designed as follows.

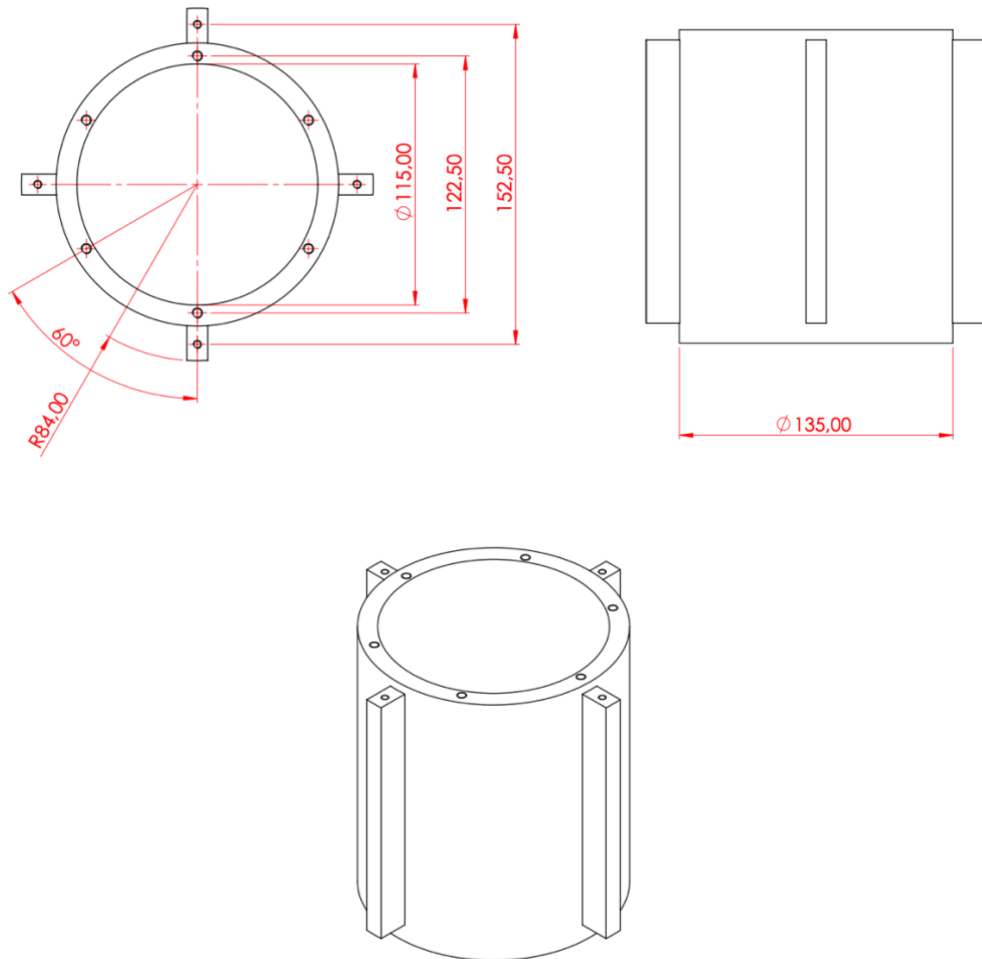


Figure 4.11 - Dynamic Test Layout, Stator 4. Design

5. This component acts as a lid to the voice coil case just described, in fact it features a hole on the top that allows the passage of the wiring of the device. Moreover, its weight contributes significantly to the total weight of 20 kg of the sprung mass. It is built of Ergal and its design is shown below.

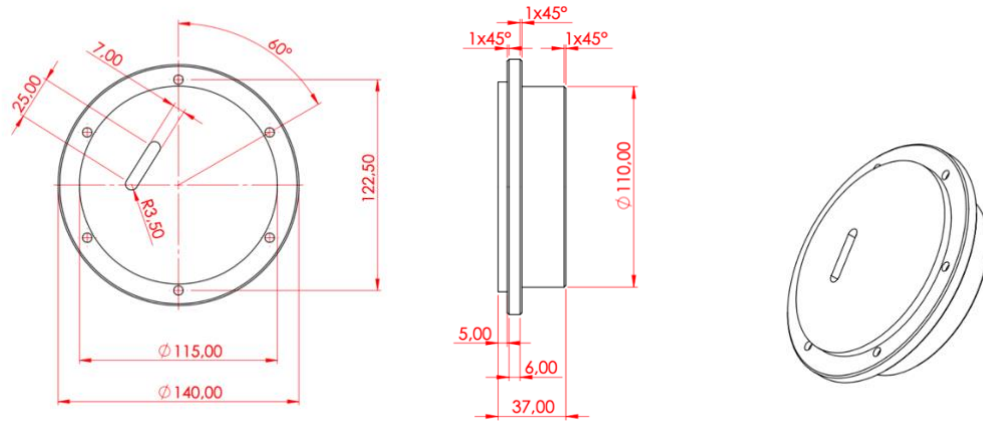


Figure 4.12 - Dynamic Test Layout, Element 5. Design

6. Four of these cross-shaped elements have the sole purpose of serving as connections sites for the two layers of springs, since they are placed between bodies 3. and 4. and they feature four brackets each. They are made of Ergal and shaped as follows.

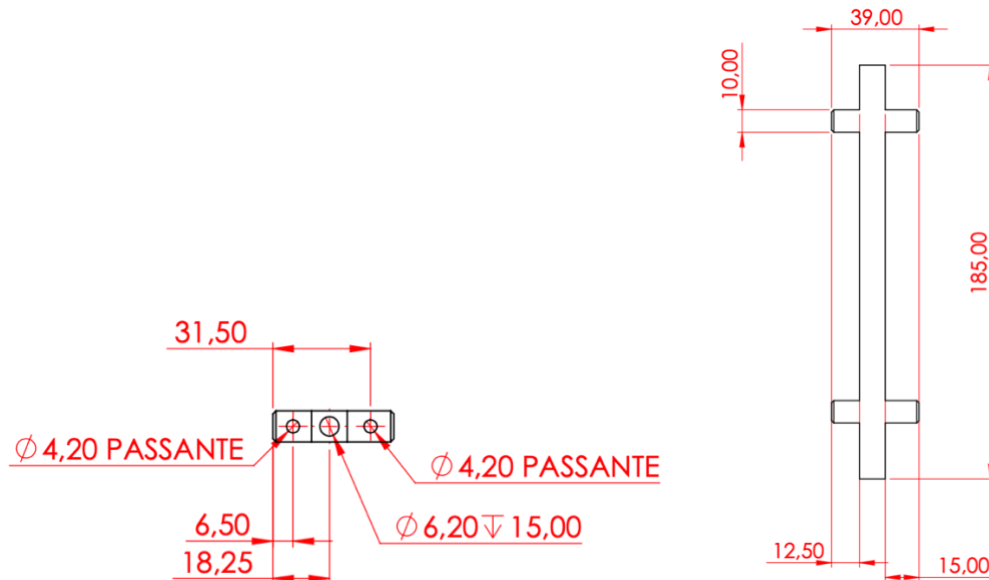


Figure 4.13 - Dynamic Test Layout, Element 6. Design

7. The external layer of springs is composed of 8 curved foil springs equally divided into two levels. They guarantee the vertical displacement in the connection between the

- unsprung mass and the stator. They are made of Lama Blu Steel and have a thickness of 1 mm. The mean diameter is equal to 202.5 mm and each swipes a 90° angle.
8. The internal layer of springs is configured like the external one and guarantees the relative vertical displacement between the sprung mass and the unsprung mass. They also are made of Lama Blu Steel and have a thickness of 0.65 mm. The mean diameter is equal to 152.5 mm and each swipes a 90° angle.
 9. The magnetic pad is the same used for the quasi-static analysis, therefore refer to p.27 (4.) for further information. Once attached to the stator the magnets cannot be moved, hence the component housing them can be mounted and used in both the test layouts. The upper part featured in the quasi-static test layout isn't needed in this arrangement. For an accurate description refer to p.29-30 (9.).
 10. The Voice Coil chosen to be implemented on the system is the Geeplus VM108-2P30-1000 [29]. The features of this device that make it suitable for this experiment are the numerous, its nominal steady state damping is equal to 481 Ns/m, superior to the optimal value formerly stated of 250 Ns/m, in addition, its maximum continuous force is higher than the load exerted by the sprung mass, leaving some margin to implement the drag force.

$$25 \frac{N}{A} \cdot 7.7A = 192.5N > 187N$$

The features of such device are described in the pictures and tables below.

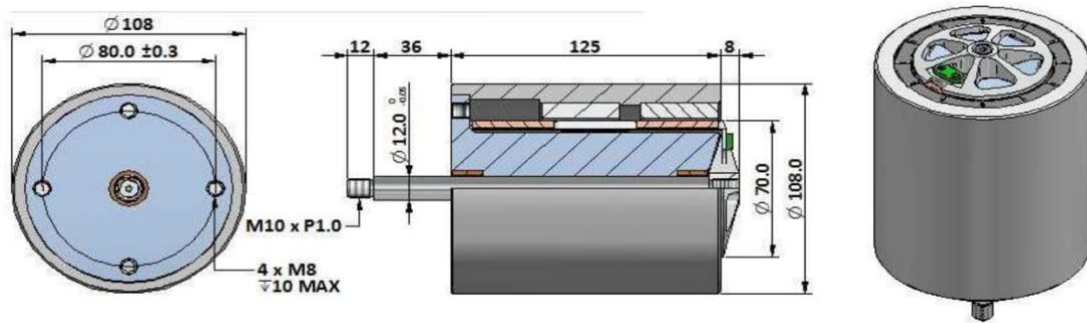


Figure 4.14 – Geeplus Voice Coil, Drawings

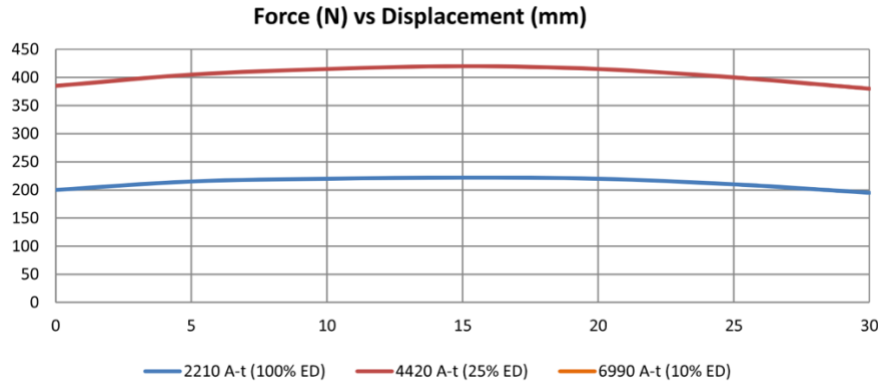


Table 4.2 – Geeplus Voice Coil Behavior

Resistance R_{20}	1.3 Ω
Inductance	N/A
Force Constant	25 N/A
Velocity Constant	25 Vs/m
Current I_{100}	7.7 A

Table 4.3 – Geeplus Voice Coil Data

Dynamic Test Layout, Modal Analysis

In this particular case a frequency analysis of the system is needed to ensure that the resonance frequencies respect the design specifics, i.e. a frequency of 3 Hz ca. for the sprung mass natural vibration mode and a frequency ranging from 10 Hz to 20 Hz for the unsprung mass natural vibration mode.

As in the previous cases, some specific parameters need to be defined before performing the analysis.

The large majority of the components of this system are chosen to be built in Ergal, an aluminum alloy with zinc as its primary alloying element. As Ergal doesn't appear on the SolidWorks list of materials, for the sake of the simulation aluminum alloy 2024-T3 is chosen, since it has similar characteristics in terms of elastic modulus and mass density. The elastic

modulus of aluminum 2024-T3 is equal to $7.24 \times 10^{10} \text{ N/m}^2$, while its mass density is equal to 2780 kg/m^3 .

Same remarks apply to the curved leaf springs, designed to be produced in Lama Blu Steel, and the magnetic pad, purchased in neodymium. To both of these components, in the CAD model, the assigned material is carbon steel, with an elastic modulus of $2.1 \times 10^{11} \text{ N/m}^2$ and a mass density coefficient equal to 7800 kg/m^3 .

Lastly, the official CAD model of the voice coil didn't provide the materials of every piece composing it so, in order to perform the simulation, a qualitative representation of the voice coil is used, and the assigned material is a copper alloy, the Nickel Silver 65-12 (UNS C75700), with elastic modulus equal to $1.25 \times 10^{11} \text{ N/m}^2$ and mass density equal to 8.690 kg/m^3 . This material is chosen for its high mass density coefficient, because the priority is to preserve the mass value of the voice coil, which equals 8 kg, and none of the other materials alone allowed to reach such mass value with this geometry.

As concerns the restraints configuration, a fixed geometry constraint was placed all over the back surface of the stator linking the system to the linear stage, the constraint simulates the behavior of the stage which has the aim of setting the initial position of the upper part of the bench with respect to the disk and prevent the relative displacement between the track and the unsprung mass.

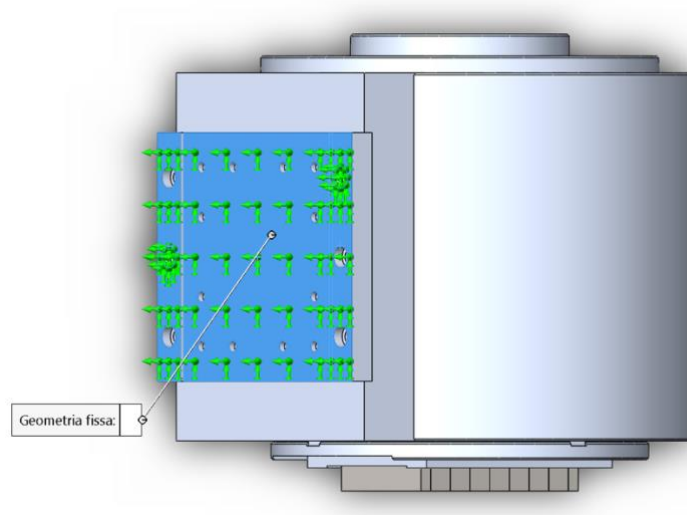


Figure 4.15 - Dynamic Test Layout, Frequency Analysis, Constraints

Finally, the mesh was generated by the software based on global element size, tolerance and mesh control, the mesh control was tuned according to the requirements of every single piece.

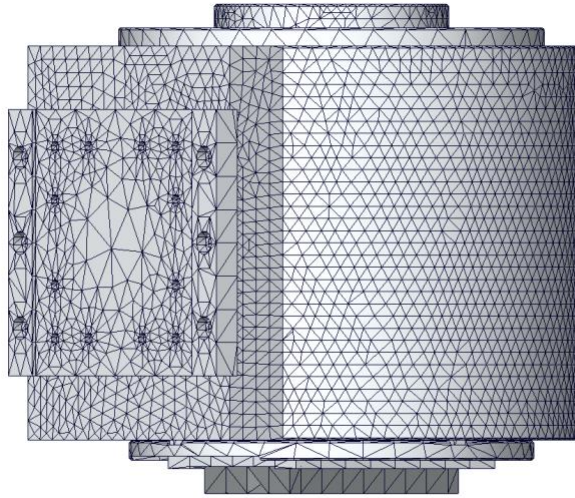


Figure 4.16 - Dynamic Test Layout, Frequency Analysis, Mesh

Once all the parameters are configured, the simulation can proceed. It has been decided to show the first 10 results, shown in ascending order of resonance frequency. In order to make the resulting natural shapes more easily appreciable, the stator surrounding the system is hidden when showing the configurations.

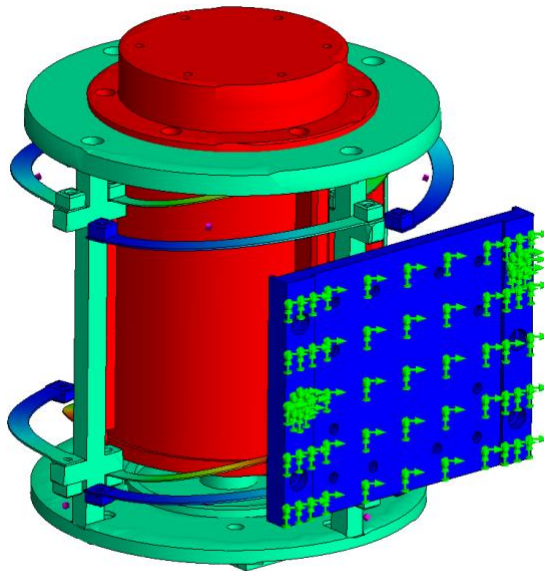


Figure 4.17 - Dynamic Test Layout, Frequency Analysis, Natural Mode 1

As it can be seen from the picture, in this configuration the unsprung mass stays nearly motionless, while the sprung mass moves. As predicted, the resonance frequency associated with this modal shape is 2.93 Hz.

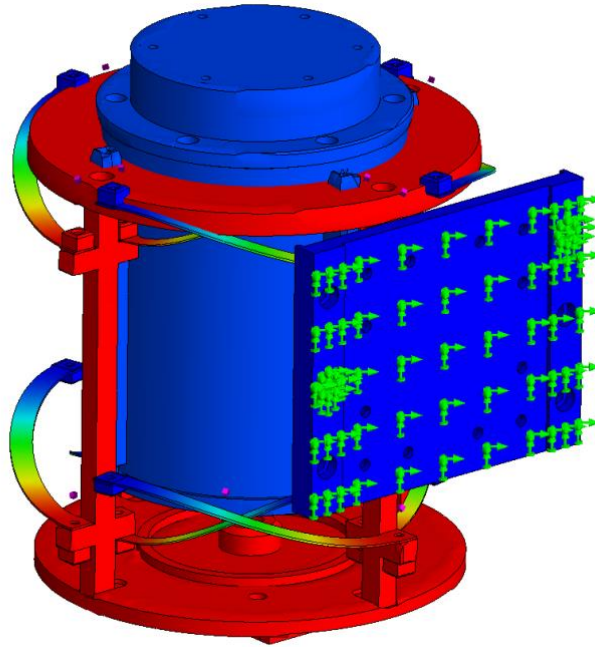


Figure 4.18 - Dynamic Test Layout, Frequency Analysis, Natural Mode 2

In this configuration the roles are inverted, the sprung mass stays unmoved while the unsprung mass displaces. As predicted, the resonance frequency associated with this modal shape is equal to 13.188 Hz.

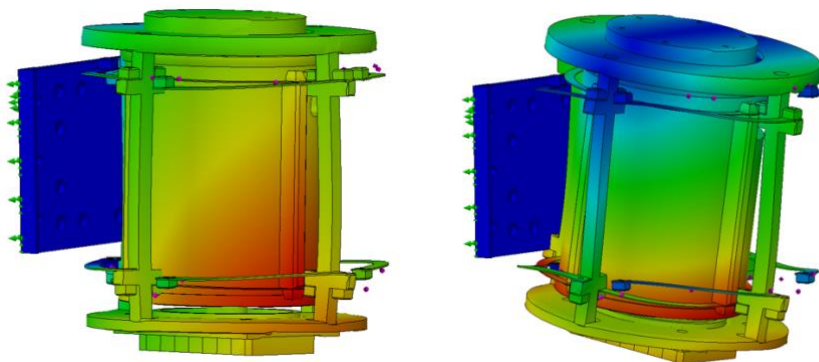


Figure 4.19 - Dynamic Test Layout, Frequency Analysis, Natural Modes 3 and 4

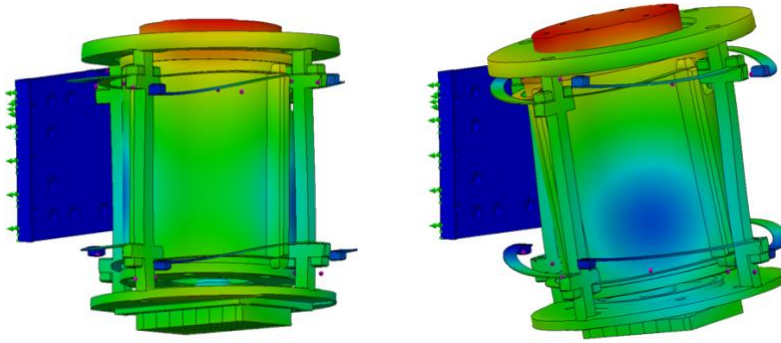


Figure 4.20 - Dynamic Test Layout, Frequency Analysis, Natural Modes 5 and 6

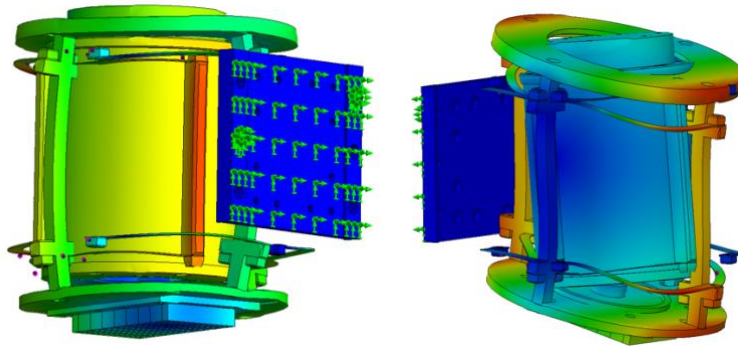


Figure 4.21 - Dynamic Test Layout, Frequency Analysis, Natural Modes 7 and 8

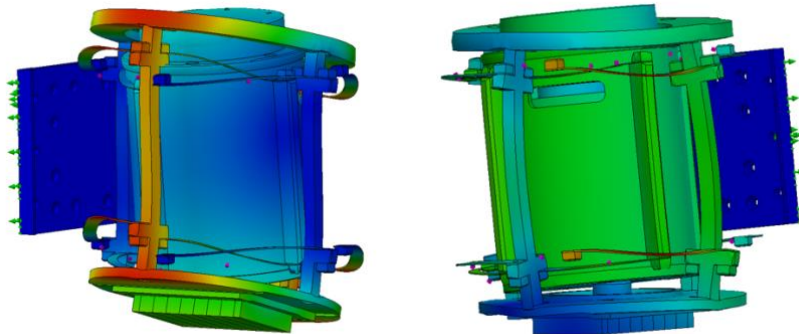


Figure 4.22 - Dynamic Test Layout, Frequency Analysis, Natural Modes 9 and 10

These last natural shapes are showed just for the sake of completeness, because the associated resonance frequencies range from 57 Hz to 246 Hz, values too high to interfere with the system dynamics to be evaluated.

As reported for the first two modal shapes, the results exactly correspond to the expectations, hence the analysis can be considered satisfactory.

Chapter 5

Next Steps, Conclusions and Further Developments

In this chapter, an overview will be given on the stages to be dealt with in the near future, namely the assembling of the dynamic test system layout and the implementation of the control strategies for the electric motor and the voice coil. Afterwards, the steps covered with this work will be retraced and further developments will be addressed.

Control Strategies

Once the systems are assembled the experiment can be carried out. To perform such experiment the electronic components of the system need to be tuned and controlled. That is the case with the electric motor and the voice coil. The control strategies for these two components will be illustrated in this section.

A rack ties the system to the power grid of 380 V and guarantees its power supply. In this rack a 3-phases driver is installed, which interacts with the motor to power it and to control it in speed. The motor in turn interacts with the bench transmitting motion.

This arrangement can be modeled as follows.

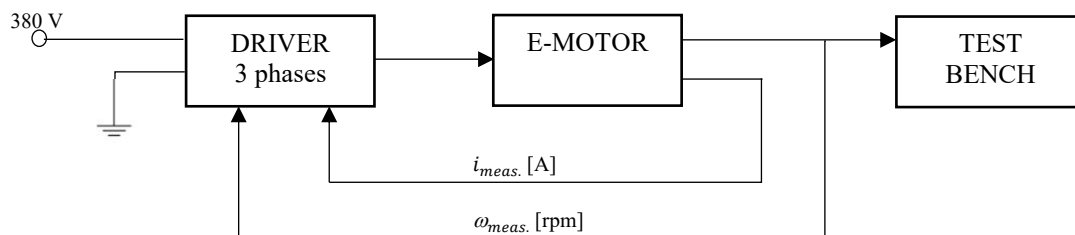


Figure 5.1 – Electric Motor Control Strategy

Down in the details of the driver-motor interaction, which is where the control action occurs, a rotational velocity ω^* input is compared to the real measured value of ω coming in feedback, resulting in an error e_ω which serves as input for the speed regulator C_ω . The purpose of C_ω is to associate a current i^* to the velocity variations exploiting the correlation between current and electromagnetic coupling. Said current i^* is compared with the measured current $i_{meas.}$ and the resulting error works as input for the controller C_I that acts directly on the plant (e -motor).

From the sensors mounted on the motor it is possible to measure the values of the current and of the torque, the former, in the form of feedback instruction, goes back to the comparison with i^* while the latter, which value, if divided by the moment of inertia of the motor, results in the measured value of the rotational speed, going as feedback to the subtraction block to be compared with ω^* and to the bench as rotational speed to which the disk rotates. The control strategy model is represented below.

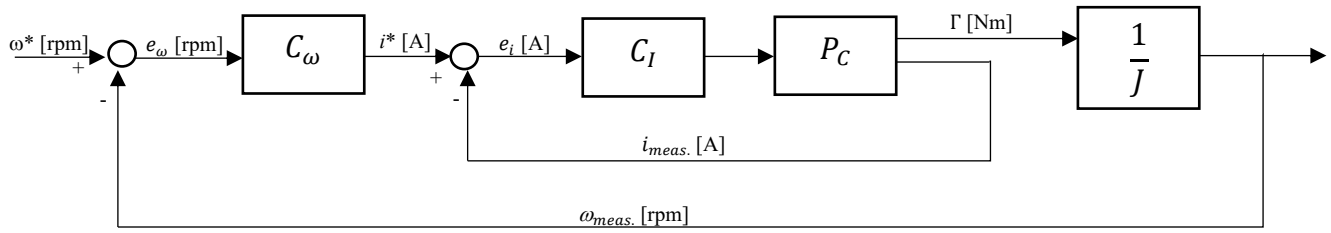


Figure 5.2 – Electric Motor Control Strategy

As for the voice coil, instead, different control strategies, increasingly precise and demanding in terms of sensors technology, can be implemented. An example of intermediate complexity is the following.

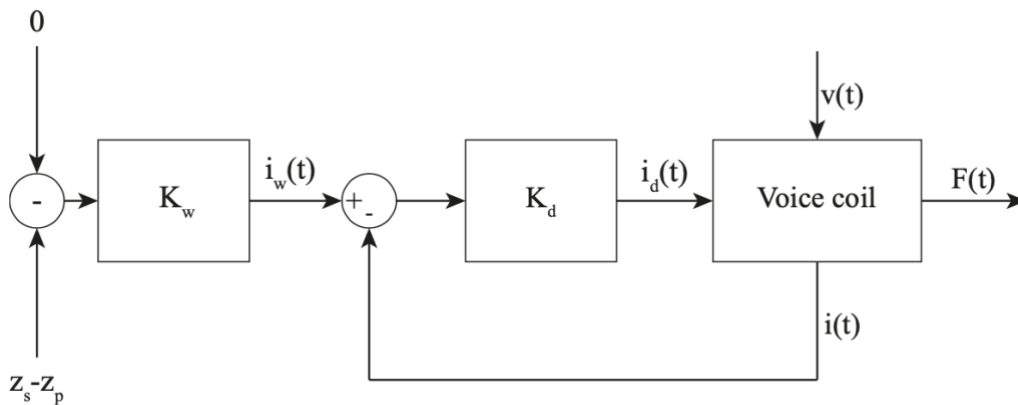


Figure 5.3 – Voice Coil Control Strategy, Courtesy of Fanigliulo, F.

In this architecture, two position sensors placed respectively on the sprung and the unsprung masses are required. These sensors detect the displacements z_s and z_p of the masses and a PI controller K_w regulates to 0 the static deformation $z_s - z_p$ of the elastic connections, as well as performing the conversion from displacement to current, as C_w did in the previous case.

The resulting $i_w(t)$ acts as a reference for the following stage, in which the voice coil current is tuned through a second PI controller K_d . This control strategy is fully functional when K_w and K_d have separate bandwidths. The output of the voice coil is the controlled damping force.

Measurement Procedures

Once both the two test layouts are assembled and the control systems implemented, it will be time to perform the measurements for which the system has been designed. The measurement procedures are different for the two test layouts.

For what concerns the quasi-static analysis, the first step consists in imposing an initial airgap between the magnetic pad and the copper track through the micrometric linear stage. Then, the motor comes into operation, transmitting to the track a counterclockwise rotation of 760 rpm. This way, the electrodynamic levitation occurs and the lift and drag forces can be measured through the designated load cells, according to the variations of the imposed airgaps. The goal is to verify that the system behaves in accordance with the simulation results reported in the following graphs.

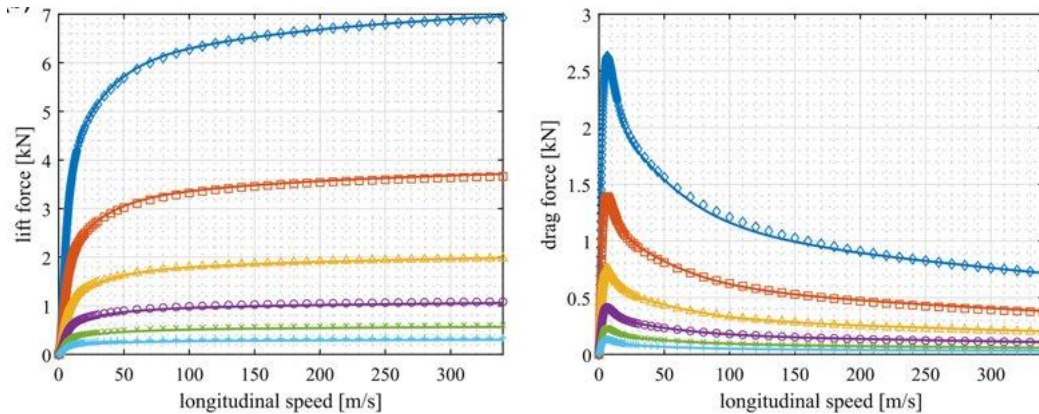


Figure 5.4 – Lift and Drag Forces Simulation Results.

As regards the dynamic test, the setup procedure is the same as for the quasi-static analysis, the initial airgap is fixed through the micrometer linear stage and a rotational speed of 760 rpm is imposed to the rotating disk by the electric motor. The purpose of this experiment is to evaluate the behavior of the system in correspondence of different values of the damping factor, tuned through the voice coil, in order to identify the optimal viscous damping to stabilize the system. The system should perform according to the simulation results shown in the following charts.

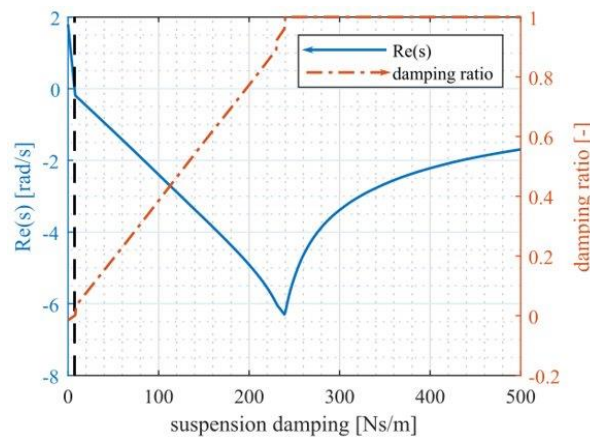


Figure 5.5 – Selection of the Optimal Damping Value

Conclusions

The urge for reducing the carbon footprint of the transportations sector, along with the need for increasingly fast and reliable travelling systems, lead, among the others, to the development of the magnetic levitation framework. The maglev technology drew significant attention thanks to its potentially zero-emissions propulsion and the high speeds it is capable to reach (600 km/h). A further step in this direction is represented by the Hyperloop technology which, introducing the concept of vacuum-sealed tubes, doubles the speed limit, raising it to 1200 km/h. This is possible because in a vacuum-sealed tube the capsule isn't subject to air friction phenomena.

Many aspects of this technology, namely the propulsion mechanism, the design and implementation of the infrastructures as well as the aerodynamic behavior of the capsules, have been thoroughly tackled by recent research work, while the enabling mechanism of this technology, the levitation subsystem, is still partially unexplored.

The passive electrodynamic technologies to exploit in order to implement capsule suspension, yield intrinsically unstable behavior. Galluzzi et al. assess the phenomenon and provide a multi-domain approach to regulate this aspect. The goal is to combine the electromagnetic domain variables describing the eddy current distribution with the mechanical domain variables describing the levitation dynamics and compensate, with additional damping, the instability of the system.

Said model is validated by Circosta et al. through a multi-degrees-of-freedom representation of the capsule.

This work deals with the design process of a test bench aimed at experimenting and validating the above discussed approach in a Hyperloop-like environment.

After identification of the Hyperloop technology within the magnetic levitation framework and a synthetic state-of-the-art analysis, the focus moves on the design specifics of every subsystem of the test rig.

Firstly, the main frame is described, design choices are motivated, every component of the system is identified and its function delineated. Static analyses and frequency analyses are performed and the results are provided and discussed.

Afterwards, the upper part of the bench is illustrated, motivating the design of two different layouts aimed at performing two different kinds of analysis and evaluating different aspects of the system. For both these test layouts accurate descriptions are presented along with components' static analyses and assemblies' frequency analyses results and discussion.

The next steps of this project consist in assembling the remaining parts of the system, the main frame and the dynamic test layout, and implementing the control strategies previously discussed. Finally it will be time to perform the experiment and collect the results, which will serve as references for further developments of this technology.

Bibliography

1. IEA, “Emissions by Sector” URL: <https://www.iea.org/reports/greenhouse-gas-emissions-from-energy-overview/emissions-by-sector> (cit. on p.1)
2. Burkhard, N., 2014, “Why Invent the Hyperloop?”, URL: <http://large.stanford.edu/courses/2014/ph240/burkhard2/> (cit. on p.2)
3. Powell, J. and Danby, G., “MAGLEV: The New Mode of Transport for the 21st Century”, 21st Century Science and Technology Magazine, Summer 2013 (cit. on p.2)
4. Lin, W., “World’s first 600 km/h high-speed Maglev Train to make Public Debut in Qingdao”, URL: <https://www.globaltimes.cn/page/202107/1228998.shtml> (cit. on p.2)
5. Galluzzi et al., “A Multi-domain Approach to the Stabilization of Electrodynamic Levitation Systems”, Journal of Vibrations and Acoustics, December 2020, vol.142 (cit. on p.2)
6. SpaceX, “Hyperloop Alpha”, 2013, URL: https://www.tesla.com/sites/default/files/blog_images/hyperloop-alpha.pdf (cit. on p.3)
7. Post, R. F. and Ryutov, D., “The Inductrack Concept: A New Approach to Magnetic Levitation”, Lawrence Livermore National Lab, CA, Technical Report UCRL-ID-124115, May 1996 (cit. on p.3, 4)
8. Nick, N., Sato, Y., “Computational Fluid Dynamics Simulation of Hyperloop Pod Predicting Laminar-Turbulent Transition”, Railway Engineering Science, 28(21), February 2020 (cit. on p.4)
9. Choi, C., Lee, K., Jo, D. J., “Sub-Sonic-Linear Synchronous Motors Using Superconducting Magnets for the Hyperloop”, Energies 12(24), December 2019 (cit. on p.4)
10. Tudor, D., Paolone, M., “Optimal Design of the Propulsion System of a Hyperloop Capsule”, IEEE Transactions on Transportation Electrification, November 2019 (cit. on p.4)
11. Tonoli, A., Amati, N., Impinna, F. and Detoni, J. G., “A Solution for the Stabilization of Electrodynamic Bearings: Modelling and Experimental Validation”, ASME J. Vib. Acoust., 133(2), 2011 (cit. on p.4)
12. Impinna, F., Detoni, J. G., Amati, N. and Tonoli, A., “Passive Magnetic Levitation of Rotors on Axial Electrodynamic Bearings”, IEEE Trans. Magn., 49(1), 2013 (cit. on p.4)
13. Tonoli, A., “Dynamic Characteristics of Eddy Current Dampers and Couplers”, J. Sound Vib., 301(3-5), 2007 (cit. on p.4)

14. Lembke, T. A., “Design and Analysis of a Novel Low Loss Homopolar Electrodynamic Bearing”, Ph.D. Thesis, School of Electrical Engineering, KTH, Stockholm, Sweden, 2005 (cit. on p.4)
15. Lembke, T. A., “Review of Electrodynamic Bearings”, ISMB14, 14th International Symposium on Magnetic Bearing, Linz Austria, Aug. 11-14, 2014 (cit. on p.4)
16. Filatov, A. and Maslen, E., “Passive Magnetic Bearing for Flywheel Energy Storage Systems”, IEEE Trans. Magn., 37(6), 2001 (cit. on p.4)
17. Chaidez, E., Bhattacharyya, S. P., Karpetis, A. N., “Levitation Methods for Use in the Hyperloop High-Speed Transportation System”, Energies, 12.21, 2019 (cit. on p.4, 5)
18. Guo, Z., Li, J., Zhou, D., “Study of a Null-Flux Coil Electrodynamic Suspension Structure for Evacuated Tube Transportation”, Symmetry, 11.10, 2019 (cit. on p.4)
19. Galluzzi, R. et al., “A Multi-Domain Approach to the Stabilization of Electrodynamic Levitation Systems”, Journal of Vibration and Acoustics, 142.6, 2020 (cit. on p.4)
20. Circosta, S. et al., “Passive Multi-Degree-of-Freedom Stabilization of Ultra-High-Speed Maglev Vehicles”, Journal of Vibration and Acoustic, 143.6, 2021 (cit. on p.4)
21. Gurol, H. et al., General Atomics Low Speed Maglev Technology Development Program (Supplemental 3), Tech. rep. United States, Federal Transit Administration, Office of Technology, 2005 (cit. on p.5)
22. Fanigliulo, F., “Design and Control of an Experimental Test System for a Linear Electrodynamic Levitation Device”, Master’s Degree Thesis, Politecnico di Torino, 2021 (cit. on p.45)
23. SKF Bearings and Mounted Products, SKF Group, Apr. 2018 (cit. on p.9)
24. AKM Servo Motor Selection Guide, Kollmorgen, URL: https://www.kollmorgen.com/sites/default/files/Kollmorgen_AKM_Servomotor_Selection_Guide.pdf
25. RW Italia, Prodotti, Giunti di Precisione, URL: <https://www.rw-italia.it/prodotti/giunti-di-precisione/giunti-a-soffietto-metallico/bk2/>
26. SolidWorks Web Help, 2019, URL: <https://help.solidworks.com/>
27. Norelem, Tables de Guidage à Queue d’Aronde Avec Vis Micrométrique, URL: https://www.norelem.fr/xs_db/DOKUMENT_DB/www/NORELEM/DataSheet/it/21/21000_Datasheet_4570_Tavole_di_guida_a_coda_di_rondine_con_vite_micrometrica--it.pdf
28. HBM, Sensori, S2 Sensori di Forza + Celle di Carico, URL: <https://www.hbm.com/it/3364/s2m-affidabili-trasduttori-di-forza-ad-s-di-alta-precisione/>
29. Geeplus Electromechanical Actuators Catalogue, 2019, URL: https://www.geeplus.com/wp-content/uploads/2019/08/Voice_Coil_motor_VM108-2P30.pdf